A mouse model for congenital myasthenic syndrome due to MuSK mutations reveals defects in structure and function of neuromuscular junctions

Frédéric Chevessier[1,*], Emmanuelle Girard[2], Jordi Molgó[3], Sönke Bartling[4], Jeanine Koenig[5,6], Daniel Hantaï[6,7] and Veit Witzemann[1]

[1]Max-Planck-Institut für Medizinische Forschung, Jahnstrasse 29, 69120 Heidelberg, Germany, [2]Inserm, U686, Biologie des Jonctions Neuromusculaires Normales et Pathologiques, 75005 Paris, France, [3]CNRS, Institut de Neurobiologie Alfred Fessard-FRC2118, Laboratoire de Neurobiologie Cellulaire et Moléculaire—UPR 9040, 91118 Gif sur Yvette, France, [4]Abteilung Medizinische Physik in der Radiologie, Deutsches Krebsforschungzentrum, 69120 Heidelberg, Germany, [5]Université Bordeaux II, 33076, Bordeaux, France, [6]Inserm, U582, Institut de Myologie, Hôpital de la Salpêtrière, 75013 Paris, France and [7]AP-HP, Centre de référence des maladies neuromusculaires Paris-Est, Hôpital de la Salpêtrière, Paris, France

In the muscle-specific tyrosine kinase receptor gene *MUSK*, a heteroallelic missense and a null mutation were identified in a patient suffering from a congenital myasthenic syndrome (CMS). We generated one mouse line carrying the homozygous missense mutation V789M in *musk* (*musk*^V789M/V789M mice) and a second hemizygous line, resembling the patient genotype, with the V789M mutation on one allele and an allele lacking the kinase domain (*musk*^V789M/− mice). We report here that *musk*^V789M/V789M mice present no obvious abnormal phenotype regarding weight, muscle function and viability. In contrast, adult *musk*^V789M/− mice suffer from severe muscle weakness, exhibit shrinkage of pelvic and scapular regions and hunchback. *Musk*^V789M/− diaphragm develops less force upon direct or nerve-induced stimulation. A profound tetanic fade is observed following nerve-evoked muscle contraction, and fatigue resistance is severely impaired upon a train of tetanic nerve stimulations. Electrophysiological measurements indicate that fatigable muscle weakness is due to impaired neurotransmission as observed in a patient suffering from a CMS. The diaphragm of adult *musk*^V789M/− mice exhibits pronounced changes in endplate architecture, distribution and innervation pattern. Thus, the missense mutation V789M in MuSK acts as a hypomorphic mutation and leads to insufficiency in MuSK function in *musk*^V789M/− mutants. These mutant mice represent valuable models for elucidating the roles of MuSK for synapse formation, maturation and maintenance as well as for studying the pathophysiology of a CMS due to MuSK mutations.

INTRODUCTION

The differentiation of the neuromuscular junction (NMJ) is a multistep process requiring coordinated interactions between nerve terminals and muscle (1,2). Signals that regulate the localization and stabilization of developing contacts are mediated by neuronal agrin and the muscle-specific receptor tyrosine kinase MuSK, that is required for the prepatterning of acetylcholine receptors (AChRs) (3–10). Nerve-secreted agrin may either induce *de novo* AChR clusters or stabilize the preformed AChRs accumulation enhancing MuSK activity, and prevent dispersion of post-synaptic specializations (6,9–10). The neurotransmitter acetylcholine induces post-synaptic AChR activity, which is necessary for the correct positioning of endplates (11), and may be also involved in the removal of excess of non-synaptic AChR clusters (12,13). MuSK signalling is also required for the stabilization and maintenance of NMJs throughout life. Indeed, the conditional inactivation of MuSK in mice

*To whom correspondence should be addressed. Tel: +49 6221486475; Fax: +49 6221486459; Email: frederic.chevessier@mpimf-heidelberg.mpg.de

during post-natal development leads to defects in NMJ maintenance and premature death (14).

Recently, Dok-7, a member of the 'downstream-of-kinase' family of cytoplasmic proteins has been shown to interact with MuSK and to modulate its activity. Mice lacking Dok-7 formed neither AChR clusters nor neuromuscular synapses confirming that this adaptor protein is essential for neuromuscular synaptogenesis through its interaction with MuSK (15). Moreover, mutations in Dok-7 identified in patients suffering from a limb-girdle congenital myasthenic syndrome (CMS), which impair MuSK activity, appear to interfere with maturation and/or maintenance of NMJs (16–19). Thus, MuSK and Dok-7 participate actively in the functional and structural integrity of NMJs in adult muscle.

CMSs are a heterogeneous group of inherited disorders of neurotransmission characterized by a fatigable muscle weakness. In these patients, the safety margin of neurotransmission is impaired by one or several mechanisms (20). A search of candidate genes has resulted in the identification of mutations in 11 genes that encode proteins of NMJ (17,21–23). Two heteroallelic mutations were discovered in *MUSK* in a patient suffering from an autosomal recessive CMS: a frameshift mutation (c.220insC) leading to the absence of MuSK expression and a missense mutation (V790M) located in the catalytic kinase domain of MuSK (24). Hemizygosity for MuSK is not a sufficient condition to induce the disease. Indeed, the father of this patient bearing the frameshift mutation did not present CMS. Moreover, $musk^{+/-}$ mice do not have any phenotypic abnormalies. Thus, to examine the pathogenicity of the missense mutation *in vivo*, we introduced the V789M (mouse homologous of the human V790M mutation) into the mouse MuSK gene by homologous recombination. We explore how this mutation by itself at homozygous state or in conjunction with an inactivated allele, as observed in the MuSK-mutated patient, alters the NMJ structure and physiology, and induces symptoms of fatigable muscle weakness. The results show that the MuSK-mutant mice represent valuable models to study mechanisms that cause a myasthenic syndrome, and to disclose the physiological role of MuSK from synapse formation to NMJ maintenance and muscle function.

RESULTS

Generation of $musk^{V789M/V789M}$ and $musk^{V789M/-}$ mice

To investigate *in vivo* the physiological consequences of MuSK mutations identified in human (24), we generated a mouse line by homologous recombination bearing the V789M mutation in the kinase domain of MuSK ($musk^{V789M/V789M}$ mice). This mutation corresponds to the mutation V790M in human MuSK at the homologous position that differs numerically due to a different numbering scheme. The basic targeting vector used in this study (Fig. 1A) has been used previously for the conditional inactivation of MuSK during post-natal development (14). Here, we replaced in exon 15, encoding the kinase domain, nucleotide G at position 2365 of the coding sequence by A (c.2365G→A; NCBI accession: NM_010944) (see Materials and Methods, Fig. 1A) and used the construct to transfect embryonic stem (ES) cells by electroporation. Heterozygous ES cells were identified by

PCR and Southern blot analysis (Fig. 1B) and the correct homologous recombination was verified by sequencing. Two independent ES cell clones were used for blastocyst transfer to generate two independent $musk^{V789M/+}$ mouse strains. Breeding of heterozygous $musk^{+/V789M}$ mice (eight independent crossings; $n = 77$ newborn mice) approximated the expected ratio of 1:2:1 of Mendelian inheritance of the genotype: $musk^{+/+}$ mice, 18% ($n = 14$); $musk^{+/V789M}$ mice, 56% ($n = 43$) and $musk^{V789M/V789M}$ mice 26% ($n = 20$). Both the mutated $musk^{V789M/+}$ and $musk^{V789M/V789M}$ mice were indistinguishable from their wild-type (WT) siblings at birth and seemed healthy during the sexual maturity stage, indicating that the V789M mutation at homozygous state is not lethal during embryonic and perinatal stages and has no impact on the general health condition at young age. The $musk^{V789M/V789M}$ mice are fertile and produce homozygous offspring.

The patient suffering from CMS (24) carries two heteroallelic mutations in *MUSK*, the missense mutation V790M in exon 15 and a null mutation in exon 3. Insertion of C at position 220 of the coding sequence (c.220insC) causes a frameshift that generates a premature stop codon and thus truncation of the gene product. To establish a corresponding mouse model, we bred the $musk^{V789M/V789M}$ mice with $musk^{+/-}$ mice to obtain hemizygous $musk^{V789M/-}$ mice that resemble the human counterpart in their genotype. Breeding of heterozygous $musk^{+/-}$ mice with $musk^{V789M/V789M}$ mice (eight independent crossings; $n = 72$ newborn mice) approximated the expected ratio of 1/2: 1/2 of Mendelian inheritance of the genotype: $musk^{V789M/+}$ mice, 45% ($n = 32$) and $musk^{V789M/-}$ mice, 55% ($n = 40$) suggesting that no particular death of $musk^{V789M/-}$ mice occurred during prenatal period.

$musk^{V789M/V789M}$ mice display no obvious abnormal phenotype, whereas $musk^{V789M/-}$ mice develop severe muscle weakness

The $musk^{V789M/V789M}$ mice presented no obvious physical signs of muscle weakness, and weight and general behaviour of these mice were normal compared with WT (Fig. 2A and B) or the $musk^{loxP/loxP}$ or $musk^{loxP/-}$ mice described previously (14).

The $musk^{V789M/-}$ mice developed, also apparently, normally during the first 3 weeks. After this period, however, changes in the trunk, pelvic and scapular regions became progressively visible to the naked eye by the reduced muscle mass, an easy perception of sacral vertebrae, the deformation of backbone and the gradually increasing kyphosis (Fig. 2C and D). The CT scan analysis performed on $musk^{V789M/-}$ mice at post-natal day (P) 45 unveiled the abnormal curvature of the spine between the thoracic and lumbar vertebrae (thoracolumbar kyphosis) compared with WT mice (Fig. 2E and F). The weakness of the pelvic muscles in these mice led most often to an abnormal walk posture characterized as a waddling gait (not shown). The delayed onset of severe muscle weakness may reflect differences in muscle development indicating that MuSK signalling occurs not in a generalized manner in all muscles. However, the $musk^{V789M/-}$ mice remained mobile. During puberty, $musk^{V789M/-}$ male mice showed a deficit in weight gain when compared with WT male mice (Fig. 2A). By 2 months of age, they exhibited ∼75% of the body weight of control littermates. As observed in the survival
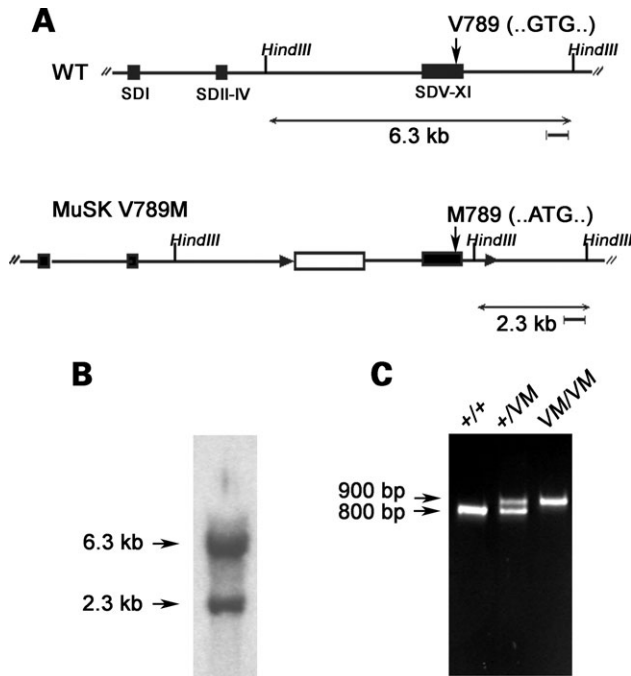
Figure 1. Gene targeting of the *musk* gene. (**A**) The upper diagram shows a simplified genomic map of the mouse *musk* gene encoding the sequences of the kinase domain (black boxes) SDI, SDII–IV and SDV–XI corresponding to the three tyrosine kinase exons according to DeChiara *et al*. (3). The G to A transition (c.2365G→A) leading to the V789M missense mutation is indicated schematically. The targeted *musk* allele (below) carrying the mutation contains a *pkg-neo* cassette (open box) and loxP sequences (arrow heads) flanking the exon encoding the catalytic part of MuSK kinase domain (14). The hybridization probe (bars below the genomic maps) used to detect the endogeneous 6.3 kb and mutant 2.3 kb *Hin*dIII-digested DNA fragments (double arrow lines). (**B**) Southern blot hybridization analysis of ES cell clone used to generate chimeric mice. The *Hin*dIII-digested fragments of 6.3 and 2.3 kb correspond to WT and *musk*^{V789M} allele, respectively. (**C**) Genotyping by PCR. DNAs prepared from tail were analysed by the 662 and 852 primers (see Materials and Methods). The 800 and 900 bp bands represent WT (+/+) and knock-in (VM) alleles, respectively.

curve (Fig. 2G), more than 40% of the male population presented a reduced life expectancy and died between the second and fourth month of life. After this period, the vital prognosis appeared stabilized for the rest of the *musk*$^{V789M/-}$ male population. Female mice were affected physically in a similar way although no premature death was noted during and after this period (Fig. 2G).

The *musk*$^{V789M/-}$ mice have abnormal locomotion activities

To investigate in the *musk*$^{V789M/-}$ mice muscle weakness and the behaviour during locomotion activities, we performed two motor tests between P18 and P60. First, we measured the grip strength of the forelimbs. No difference was then observed in grip strength between homozygous *musk*$^{V789M/V789M}$ mice and WT mice during this period (Fig. 2H). In contrast, the grip strength of the *musk*$^{V789M/-}$ mice was progressively reduced beyond P21. At P60, forelimb grip strength was reduced by 30% compared with WT (Fig. 2H).

The motor coordination and the balance of the mice were tested using the Rotarod assay. After a training period of 5

days, *musk*$^{V789M/V789M}$ mice as well as the WT mice were able to maintain their balance up to 5 min on the rotating and accelerating drum (Fig. 2I). The *musk*$^{V789M/-}$ mice revealed clear deficits in this test and fell 2–3 min earlier from the drum (Fig. 2I), thus maintaining their balance only by half the normal duration time. In both tests, no difference between male and female *musk*$^{V789M/-}$ mice was observed.

Muscle contraction and neurotransmission in MuSK mutants

The most conspicuous phenotypic difference between WT or *musk*$^{V789M/+}$ and *musk*$^{V789M/-}$ mice was the reduction in body weight, the kyphosis and reduced motor performance with age. As *musk*$^{V789M/+}$ and WT mice did not show phenotypic differences, we used *musk*$^{V789M/+}$ mice as controls having the same age and genetic background as *musk*$^{V789M/-}$ littermates. To elucidate whether the cause of the motor deficits observed in *musk*$^{V789M/-}$ mice was due to impaired neuromuscular transmission, we investigated using P90 isolated *musk*$^{V789M/+}$ and *musk*$^{V789M/-}$ mouse diaphragms twitches and tetanic contractions following direct (muscle) or indirect (phrenic nerve) stimulation at different frequencies. Fatigue strength was also evaluated after a train of tetanic stimulations (Fig. 3).

Musk$^{V789M/+}$ mouse diaphragm developed and maintained similar tetanic contractions on muscle stimulations (Fig. 3A1) as observed in WT muscle (not shown). Train of tetanic muscle stimulations induced a similar degree of fatigue in *musk*$^{V789M/+}$ and *musk*$^{V789M/-}$ muscles, despite the fact that *musk*$^{V789M/-}$ hemidiaphragms developed less force than *musk*$^{V789M/+}$ ones (Fig. 3A1). In *musk*$^{V789M/-}$ mice, the strength of muscle twitch upon direct stimulation was significantly smaller than in *musk*$^{V789M/+}$ mice, both upon single and tetanic direct stimulation (Fig. 3A and Table 1). Moreover, the time to peak or contraction time (CT), and the half relaxation time (RT$_{1/2}$) of direct-evoked single twitches were significantly prolonged (Table 1).

Contraction elicited by a single or tetanic nerve stimulation in muscle of *musk*$^{V789M/+}$ mice was similar to muscle-stimulated contractions (Fig. 3B1). In *musk*$^{V789M/-}$ mice, the peak amplitude of nerve-evoked single twitch was not found significantly reduced compared with muscle stimulation, but the CT and RT$_{1/2}$ were also prolonged (Fig. 3B and Table 1). Tetanic nerve stimulation or a train of indirect tetanic stimulations of *musk*$^{V789M/-}$ hemidiaphragm produced a completely different behaviour. Indeed, this muscle was not able to maintain unique tetanic contractions (tetanic fade) or repetitive tetanic contractions suggesting that the fatigue resistance after nerve stimulation was strongly reduced (Fig. 3B and B1). Moreover, the twitch/tetanus ratio in *musk*$^{V789M/-}$ hemidiaphragm after nerve stimulation was doubled compared with *musk*$^{V789M/+}$ mouse diaphragm (Table 1).

Intracellular recordings from isolated hemidiaphragms of P90 male mice demonstrated significantly impaired neuromuscular transmission in *musk*$^{V789M/-}$ mice compared with *musk*$^{V789M/+}$ mice (Fig. 3C and D). The mean peak amplitude (around 0.8 mV) and the kinetic parameters of the miniature endplate potentials (MEPPs) of hemidiaphragms from *musk*$^{V789M/-}$ mice were comparable to *musk*$^{V789M/+}$ hemidiaphragms but of reduced frequency (Fig. 3C and Table 2).
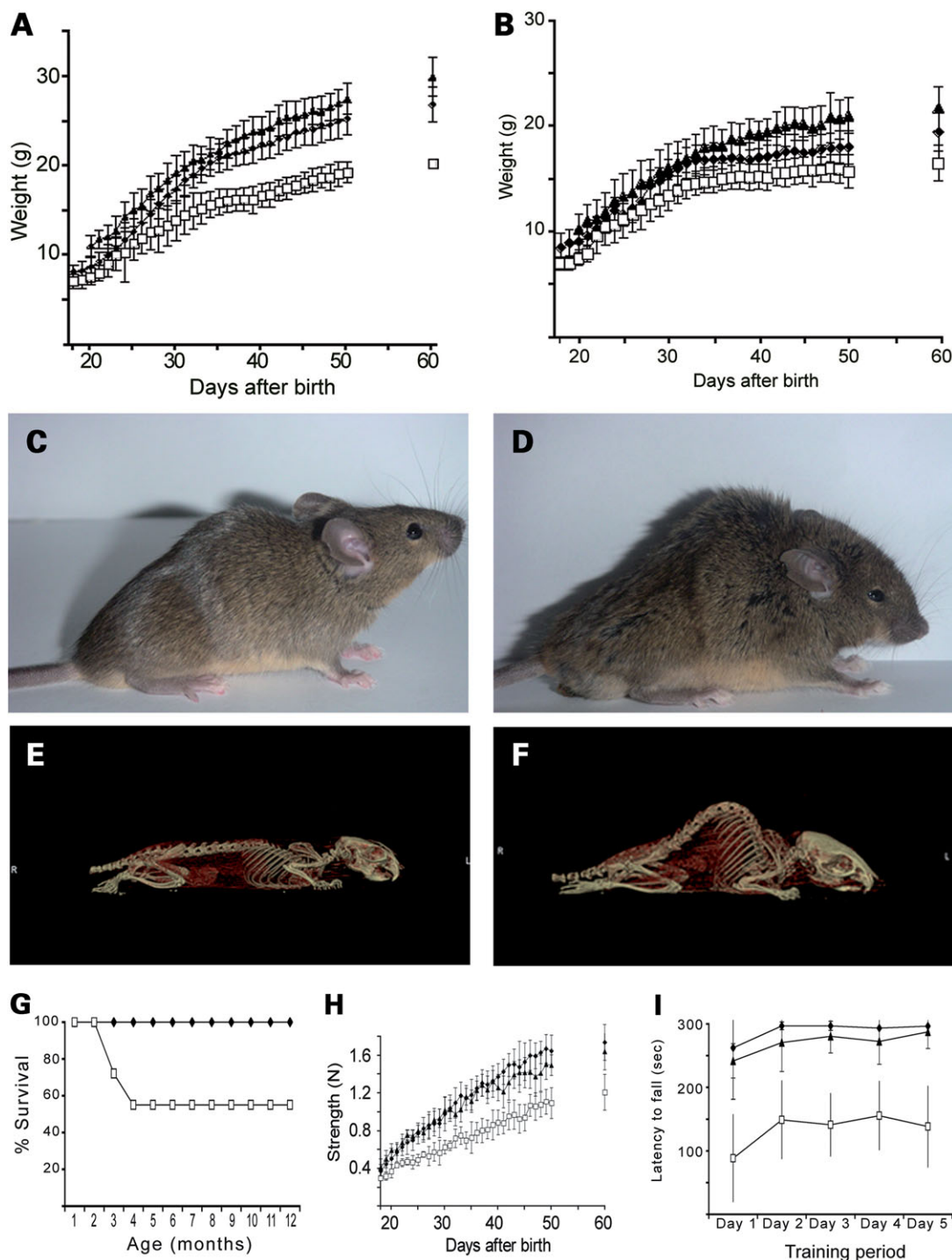
Figure 2. Overall phenotype of the $musk^{V789M/-}$ mice. (**A**) Growth curves of male mice: control (closed diamonds, $n = 20$), $musk^{V789M/-}$ (open squares, $n = 10$) and $musk^{V789M/V789M}$ (closed triangles, $n = 10$). Male $musk^{V789M/-}$ mice show a significant reduction of the body weight starting after 28 days of age. Values are means $\pm$ SD at P60, WT mice: 26.94 $\pm$ 2.1 g; ***$musk^{V789M/-}$ mice: 20.1 $\pm$ 0.6 g (***$P \leq 0.001$). (**B**) Growth curves of female mice: control (closed diamonds, $n = 17$), $musk^{V789M/-}$ (open squares, $n = 13$) and $musk^{V789M/V789M}$ (closed triangles, $n = 12$). Female $musk^{V789M/-}$ mice have a slight reduction of the body weight. Values are means $\pm$ SD at P60, WT mice: 19.52 $\pm$ 1.82 g; **$musk^{V789M/-}$ mice: 16.58 $\pm$ 1.65 g (**$P \leq 0.01$). Pictures of the same $musk^{V789M/-}$ male mouse at P40 (**C**) and P75, 1 day before the death of the animal (**D**). CT scan analysis of WT (**E**) and $musk^{V789M/-}$ (**F**) adult mice. Note the shrinkage of the pelvic and scapular region as well as the appearance of a thoracolumbar kyphosis in $musk^{V789M/-}$ mice. (**G**) Survival curve of mice: female $musk^{V789M/-}$ mice (closed diamonds, $n = 15$); male $musk^{V789M/-}$ mice (open squares, $n = 18$). More than 40% of the male $musk^{V789M/-}$ mouse population died between the second and the fourth month. (**H**) Forelimb strength (measured in Newton, N) between P18 and P60: WT mice (closed diamonds, $n = 21$), $musk^{V789M/-}$ mice (open squares, $n = 13$) and $musk^{V789M/V789M}$ mice (closed triangles, $n = 9$). Following data are means $\pm$ SEM at P60, WT mice: 1.74 $\pm$ 0.19 N; $musk^{V789M/V789M}$ mice: 1.64 $\pm$ 0.193 N ($P = 0.61$ versus WT by t-test); **$musk^{V789M/-}$ mice: 1.21 $\pm$ 0.19 N (**$P \leq 0.01$ versus WT by t-test). (**I**) Rotarod assays performed over 5 days training period in WT mice (closed diamonds, $n = 13$), $musk^{V789M/V789M}$ mice (closed triangles, $n = 9$; $P = 0.78$ versus WT by t-test) and $musk^{V789M/-}$ mice (open squares, $n = 5$; ***$P \leq 0.001$ versus WT by t-test). No difference between male and female $musk^{V789M/-}$ mice was found for both tests.

We found that the amplitudes of the full-sized endplate potentials (EPPs) were significantly decreased in the hemizygous mice, and were 76% of the control value (Fig. 3D and Table 2). Moreover, the steady-state number of quanta released by a single nerve impulse (mean quantal content) was only 61% of the control value (Table 2).

Aberrant endplate distribution and exuberant axonal growth in the diaphragm of adult *musk*[V789M/−] mice

We studied synapse distribution in P45 diaphragm muscles, because its thin structure allows visualizing synaptic contacts and the innervation pattern in whole-mount preparations with a high spatiotemporal resolution. The primary trunk of the intramuscular phrenic nerve, stained with anti-neurofilament (NF) 150 kDa antibodies, extended to the central region of the muscle and was oriented perpendicular to the long-axis of the muscle fibres (Fig. 4A). Nerve terminals normally were located at the ends of short secondary and tertiary branches growing laterally off the primary nerve trunks (Fig. 4E and G). AChRs, visualized by staining with rhodamine-conjugated a-bungarotoxin (r-bgt), were clustered in the muscle membrane at the synaptic contact sites, located as a characteristic 'endplate band' at the centre of each hemidiaphragm (Fig. 4C) and endplates are contacted by nerve terminals in WT (Fig. 4F and G). A similar innervation pattern was observed in *musk*[V789M/V789M] and *musk*[loxP/−] mice (data not shown).

In P45 male and female *musk*[V789M/−] mice, the diaphragm was notably thinner compared with *musk*[V789M/V789M] mice or WT mice (data not shown) and the innervation pattern of the diaphragm was markedly altered. The axon branches were much longer and extended from the main nerve trunk to the medial and/or lateral side of the muscle (Fig. 4B). At higher magnification, this axonal overgrowth and increased branching is evident (Fig. 4H and J). The length of the secondary neurites arising from the primary nerve trunk was measured in the upper regions of the diaphragms from WT and *musk*[V789M/−] mice (Fig. 4K).

The well-defined central endplate band was absent in *musk*[V789M/−] mouse diaphragm at P45 (Fig. 4D, I and J). The AChR clusters were, instead, scattered over a wide territory in comparison to *musk*[V789M/V789M] mice or WT mice. The different endplate distributions in WT, *musk*[V789M/V789M] and *musk*[V789M/−] mice were quantitatively evaluated by measuring the width of the endplate region at P25 (Fig. 4L). After P25, it was no longer possible to detect endplates reliably in *musk*[V789M/−] mice because of the remodelling of the endplates and the highly variable spread of the AChR clusters across the diaphragm (see later, Fig. 4L).

Remodelling of individual NMJS in the diaphragm of adult *musk*[V789M/−] mice

We analysed the pre- and post-synaptic molecular architecture of NMJs at P45 by double labelling WT, *musk*[V789M/V789M] or *musk*[V789M/−] mouse diaphragm muscles with r-bgt and anti-NF 150 kDa antibodies (Fig. 5) or anti-synaptophysin antibodies (Fig. 6). Both in WT (Fig. 5A−C) and *musk*[V789M/V789M] mice (Fig. 5D−F), axonal branches inner-

vated the well-defined and 'Pretzel'-like shaped post-synaptic structure. In *musk*[V789M/−] mouse diaphragm, however, we observed axonal sprouting and retraction bulbs (Fig. 5G, I, J and L). The r-bgt-stained AChRs were no longer concentrated in characteristic 'Pretzel'-like structures as observed in WT or *musk*[V789M/V789M] mice (Fig. 5B and E). Instead, the endplates seemed smaller than in WT mice and AChR clusters showed a highly disrupted pattern (Fig. 5K and L).

Synaptophysin staining (Fig. 6) demonstrated that AChRs were located in precise alignment with the presynaptic nerve terminal in WT (Fig. 6A−C) and *musk*[V789M/V789M] mice (Fig. 6D−F). In *musk*[V789M/−] mice, the nerve terminals appeared also apposed to AChR patches indicating that synaptic contact regions existed but their size was strongly reduced due to the high fragmentation of endplates (Fig. 6G−L). Quantification of r-bgt-stained areas revealed a significant reduction in the surface area covered by AChR clusters at NMJs of adult *musk*[V789M/−] mice compared with WT littermates [WT: $227.3 \pm 26 \ \mu m^2$; **musk*[V789M/−]: $143.85 \pm 31.65 \ \mu m^2$; $n = 30$ endplates, $n \geq 2$ mice per genotype; *$P \leq 0.05$ (*t*-test)].

Endplate evolution during post-natal maturation in the diaphragm of *musk*[V789M/−] mice

It has been previously shown that MuSK/rapsyn and agrin/ MuSK/rapsyn pathways are required for the initiation of synaptogenesis and for the synaptic differentiation during development. Indeed, mice lacking either, MuSK, the MuSK effector Dok-7, agrin or rapsyn, die at birth. They all show defects in NMJ formation or stabilization, and aberrant nerve growth (3−6,15).

As the central endplate band and the axonal length from the main nerve trunk were found highly perturbed in the diaphragm of adult *musk*[V789M/−] mice, we asked whether these modifications were already present during the early post-natal period and analysed diaphragms from WT and *musk*[V789M/−] mice at P0 up to P45 (Fig. 7). At low magnification r-bgt-stained endplate receptors were barely detectable at P0 in *musk*[V789M/−] mice suggesting that the AChR densities or the size of the endplates were reduced comparable with WT (Fig. 7A and I). Apparent increased fluorescent intensities were indicated at P5 (Fig. 7J) that decreased, however, at later stages again (Fig. 7K and L). Whether the transient increase in AChR density could be due to developmentally regulated embryonic-to-adult channel conversion or/and to the change in metabolic stability of the endplate receptors that occurs during early post-natal development needs further experiments. At higher magnification, endplate AChRs could be clearly visualized at all stages (Fig. 7M−P). Compared with WT, or *musk*[V789M/V789M] and *musk*[loxP/−] mice, the size of the endplates at P0 indeed was significantly reduced (Fig. 7Q). We also noticed that the endplates were not concentrated around a central endplate band as characteristically observed in WT (Fig. 7A−D) but were spread out over a wide range (Fig. 7I−L).

During the first two post-natal weeks, NMJs mature. AChR-rich post-synaptic apparatuses are transformed gradually but asynchronously from small oval plaques into perforated
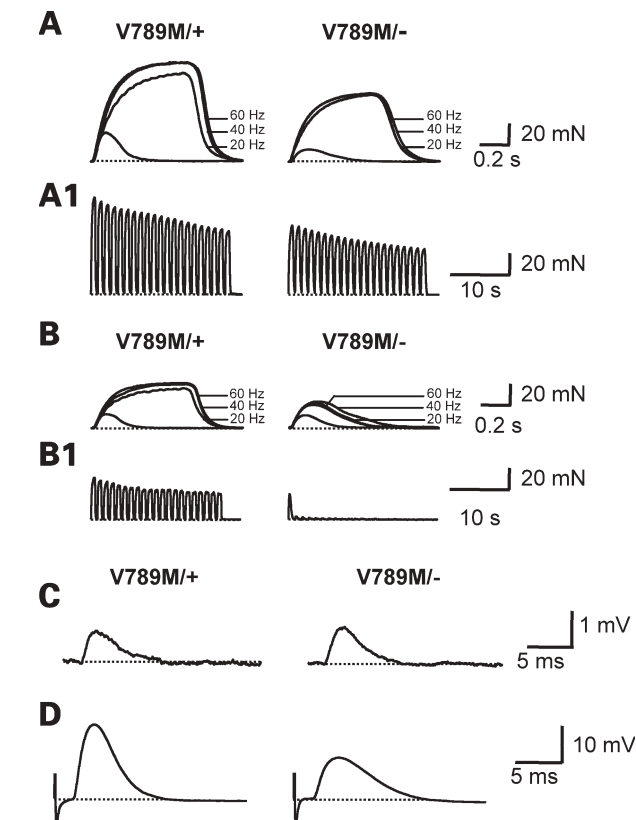
Figure 3. Muscle contraction and neurotransmission in MuSK mutants. Representative examples of twitch and tetanic contractions evoked either by direct electrical stimulation (**A** and **A1**) or by stimulating the motor nerve (**B** and **B1**) in $musk^{V789M/+}$ (left panel) and $musk^{V789M/-}$ (right panel) P90 isolated mouse hemidiaphragms. The muscle (A and A1) or the phrenic nerve (B and B1) were stimulated either with single or tetanic stimuli (600 ms duration) at 20, 40 and 60 Hz. The interval between trains was 30 s. Note in (A1) that repeated tetanic direct muscle stimulation (40 Hz, 600 ms duration at 1 Hz) induced a similar degree of fatigue in $musk^{V789M/+}$ and $musk^{V789M/-}$ muscles, despite the fact that $musk^{V789M/-}$ muscles developed less force than $musk^{V789M/+}$ ones. Note in (**B**), that $musk^{V789M/-}$ hemidiaphragms were not able to maintain tetanic contractions evoked by single nerve stimulation (20–60 Hz), or by trains of tetanic stimulation (**B1**), when compared with $musk^{V789M/+}$ muscles. Calibration scales in right panels apply to left ones. Representative traces of MEPPs (**C**) and full-sized EPPs (**D**) recorded in a $musk^{V789M/+}$ and a $musk^{V789M/-}$ hemidiaphragm muscle bathed in standard physiological solution supplemented with μ-conotoxin GIIIB to block muscle sodium channels. Notice that the EPP amplitude is reduced in the $musk^{V789M/-}$ when compared with the $musk^{V789M/+}$ muscle.

Table 1. Muscle tension parameters determined in $musk^{V789M/+}$ and $musk^{V789M/-}$ hemidiaphragms

	V789M/$^+$	SEM	V789M/$^-$	SEM
Nerve stimulation				
Peak amplitude (mN)	12.55	0.73	10.76	1.94
mN/g	115.55	3.21	79.57*	14.36
Twitch/tetanus ratio (40 Hz)	0.34	0.02	0.61*	0.03
Time to peak (ms)	96.02	1.64	122.3*	7.35
Half relaxation time (ms)	82.59	6.99	281.1*	52.38
Direct stimulation				
Peak amplitude (mN)	25.53	0.54	7.91**	0.84
mN/g	235.06	4.96	58.46**	6.24
Twitch/tetanus ratio (40 Hz)	0.26	0.02	0.31	0.03
Time to peak (ms)	87.48	4.22	127*	7.05
Half relaxation time (ms)	80.93	14.58	357.33**	31.02

Data obtained from three different $musk^{V789M/+}$ and $musk^{V789M/-}$ age-matched animals.
$^*P < 0.05$; $^{**}P < 0.0005$.

Table 2. Synaptic transmission parameters recorded in $musk^{V789M/+}$ and $musk^{V789M/-}$ hemidiaphragms

	MEPP frequency (s^{-1})	MEPP amplitude (mV)	EPP amplitude (mV)	Quantal content
V789M/$^+$	0.91	0.82	19.38	28.32
SEM	0.18	0.011	0.5	4.30
V789M/$^-$	0.27*	0.83	14.80*	17.35**
SEM	0.08	0.02	0.49	0.63

Data obtained from three different $musk^{V789M/+}$ and $musk^{V789M/-}$ age-matched animals.
$^*P < 0.005$; $^{**}P < 0.0005$.

post-synaptic apparatus (Fig. 7S). Later on, by P45, most of the endplates underwent a profound remodelling (Fig. 7P).

Muscles respond differently to mutation in MuSK

We then asked whether the remodelling of NMJs first observed in the diaphragm of $musk^{V789M/-}$ mice can be generalized to all muscles and compared the NMJ architecture of the diaphragm, intercostal, *soleus*, *extensor digitorum longus* (EDL) or *tibialis anterior* (TA) muscles (Fig. 8). We observed that diaphragm, intercostal as well as TA muscles of P45 $musk^{V789M/-}$ mice showed severe changes in post-synaptic structure and AChR distribution (Figs 5G–L and 8B and D, respectively) compared with WT mice (Figs 5A–C and 8A and C). The NMJs of these muscles showed a strong and progressive loss of AChRs leading to the fragmentation of the characteristic 'Pretzel'-like structures. At a similar stage in EDL and *soleus* muscles, 'Pretzel'-like-structures appeared less-affected (Fig. 8F and H, respectively) and largely resembled endplates of WT muscle (Fig. 8E and G). At older age, however, structural alterations (reduction of endplate receptor density and fragmentation) were also observed as shown for a P120 *soleus* muscle (Fig. 9A and B).
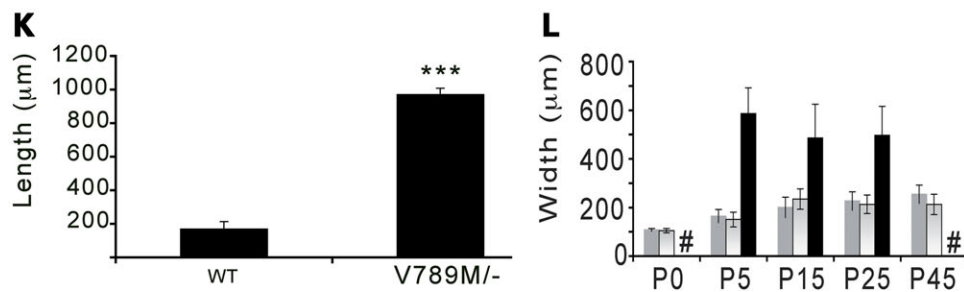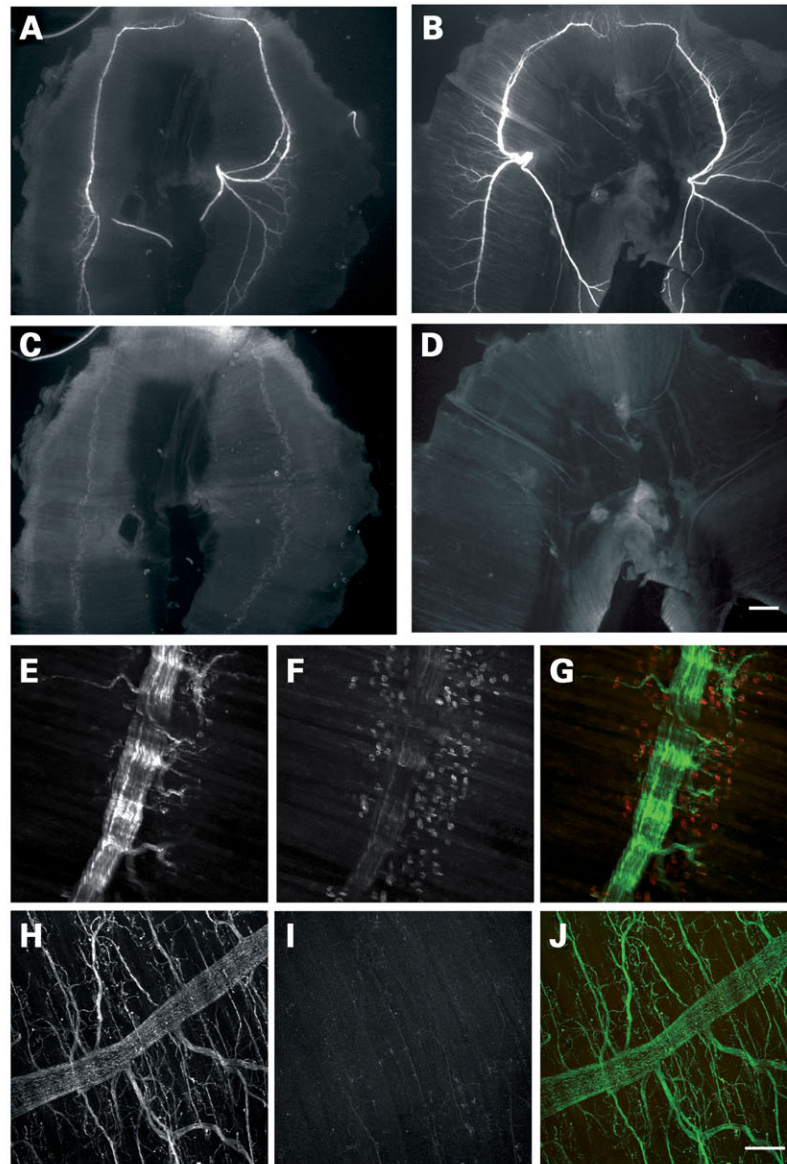
and then branched 'Pretzel-like' endplates (25–27; Fig. 7E–H and S).

Endplates in $musk^{V789M/-}$ mouse diaphragm varied at all stages from endplates in WT diaphragm. At P15, most of NMJs observed in WT mice presented compact but multi-perforated or branched-shape configurations. We noted, first, that the number of detectable AChR clusters was notably reduced in the diaphragm of $musk^{V789M/-}$ mice compared with control mice (Fig. 7C, K and R). At this stage one could still detect NMJs that appeared normal comparing AChR densities, perforation and branching of endplate regions. Other NMJs, however, displayed progressive loss of AChR-rich domains and/or complete dislocation of the

Figure 4. Absence of central AChR endplate band and neurite outgrowth in adult *musk*[V789M/−] mouse diaphragm. Whole mount preparation was performed on P45 WT (**A**, **C**, **E**−**G**), and *musk*[V789M/−] (**B**, **D** and **H**−**J**) diaphragms. Motor nerves were visualized using anti-neurofilament 150 antibodies (A, B, E and H) and endplates by labelling AChR with r-bgt (C, D, F and I). Merged images (G and J). Scale bar (A−D)=1 mm and scale bar (E−J) = 150 μm. Similar results were found for male and female *musk*[V789M/−] mice. (**K**) Length of secondary neurites extending from the primary main nerve trunk to the medial or lateral side of the muscle. Values are means ± SEM from three diaphragms per genotype: WT mice: 168.31 ± 45.3 μm; *musk*[V789M/−] mice: 969.43 ± 38.94 μm (***$P \leq 0.001$ versus WT by *t*-test). (**L**) Width of the central endplate band evaluated from birth (P0) to P45. WT mice: grey column, *musk*[V789M/V789M] mice: white column, *musk*[V789M/−] mice: black column. #: not determined.
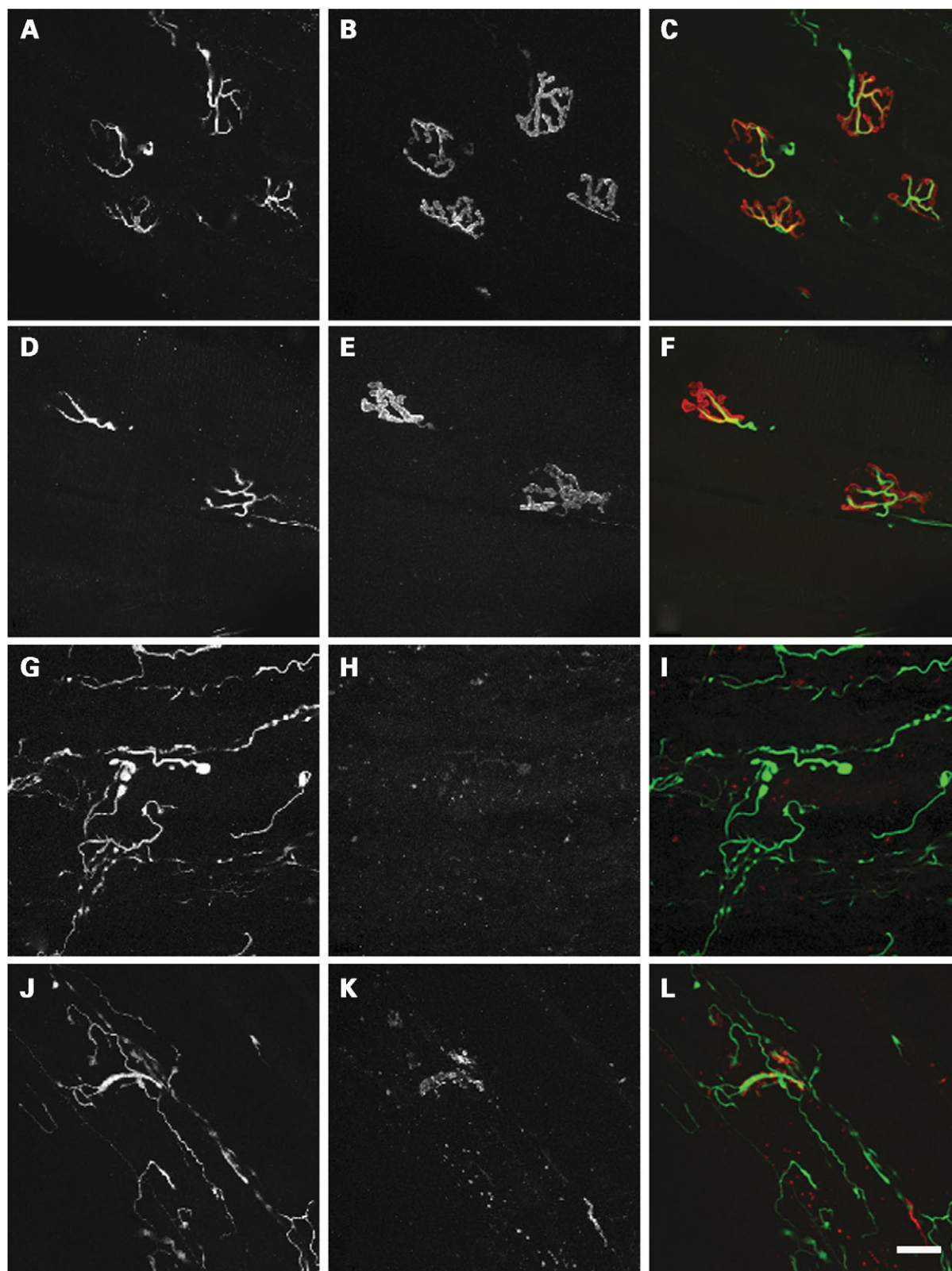
Figure 5. NMJs in diaphragms of adult WT and *MuSK* mutant mice. NMJs from WT (**A**–**C**), *musk*[V789M/V789M] (**D**–**F**), and *musk*[V789M/−] (**G**–**L**) mouse diaphragms at P45. Motor nerves are visualized using anti-neurofilament 150 antibodies (A, D, G and J) and endplates by labelling AChR with r-bgt (B, E, H and K). Merged images (C, F, I and L). Scale bar=20 μm.
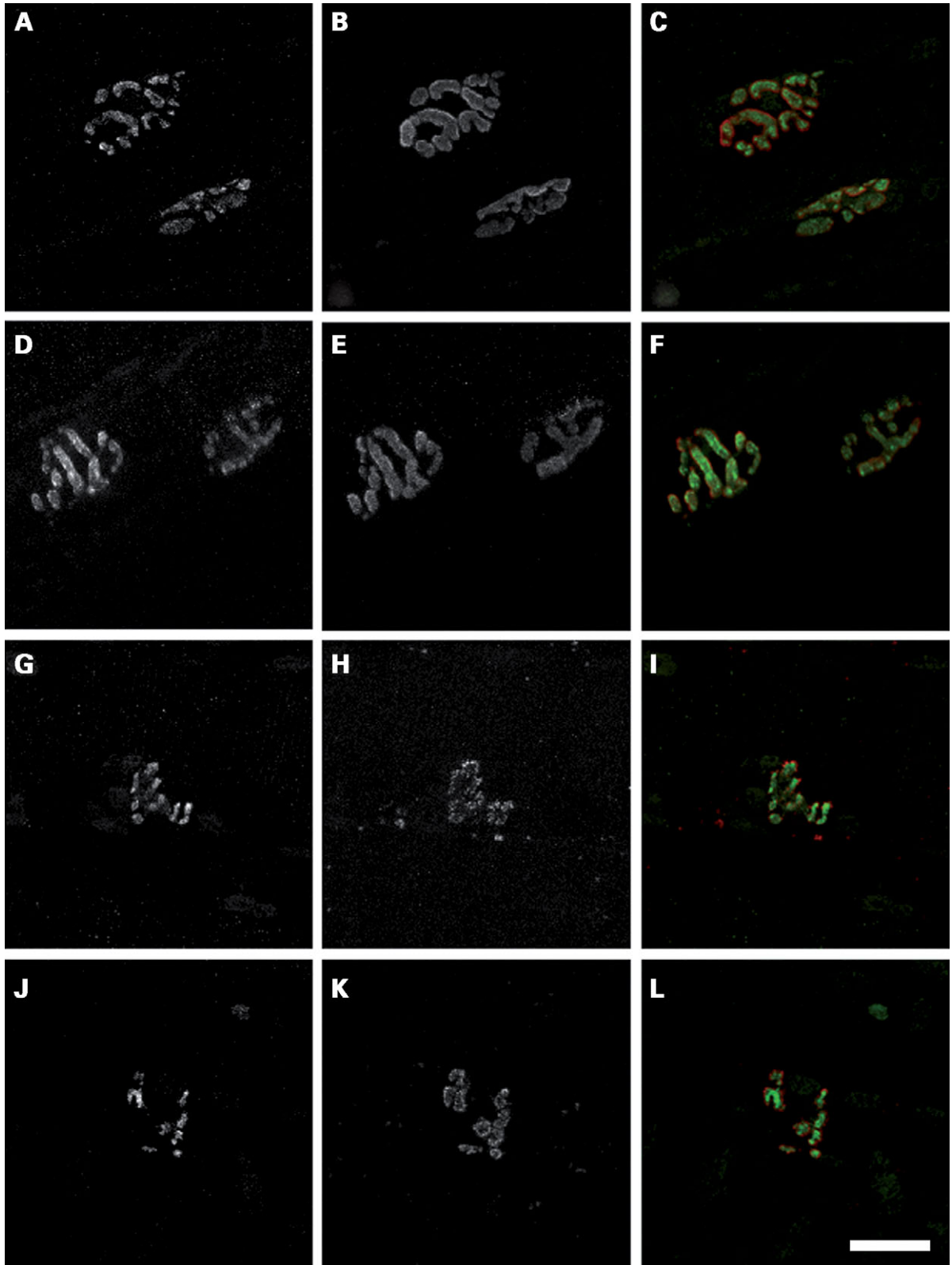
Figure 6. Presynaptic terminal size in correlation to the size of endplates in diaphragm of WT and MuSK mutant mice. NMJs from WT (**A**–**C**), *musk*$^{V789M/V789M}$ (**D**–**F**) and *musk*$^{V789M/-}$ (**G**–**L**) mouse diaphragms at P45. Nerve terminal are visualized using anti-synaptophysin antibodies (A, D, G and J) and endplates by labelling with r-bgt (B, E, H and K). Merged images (C, F, I and L). Scale bar = 20 μm.
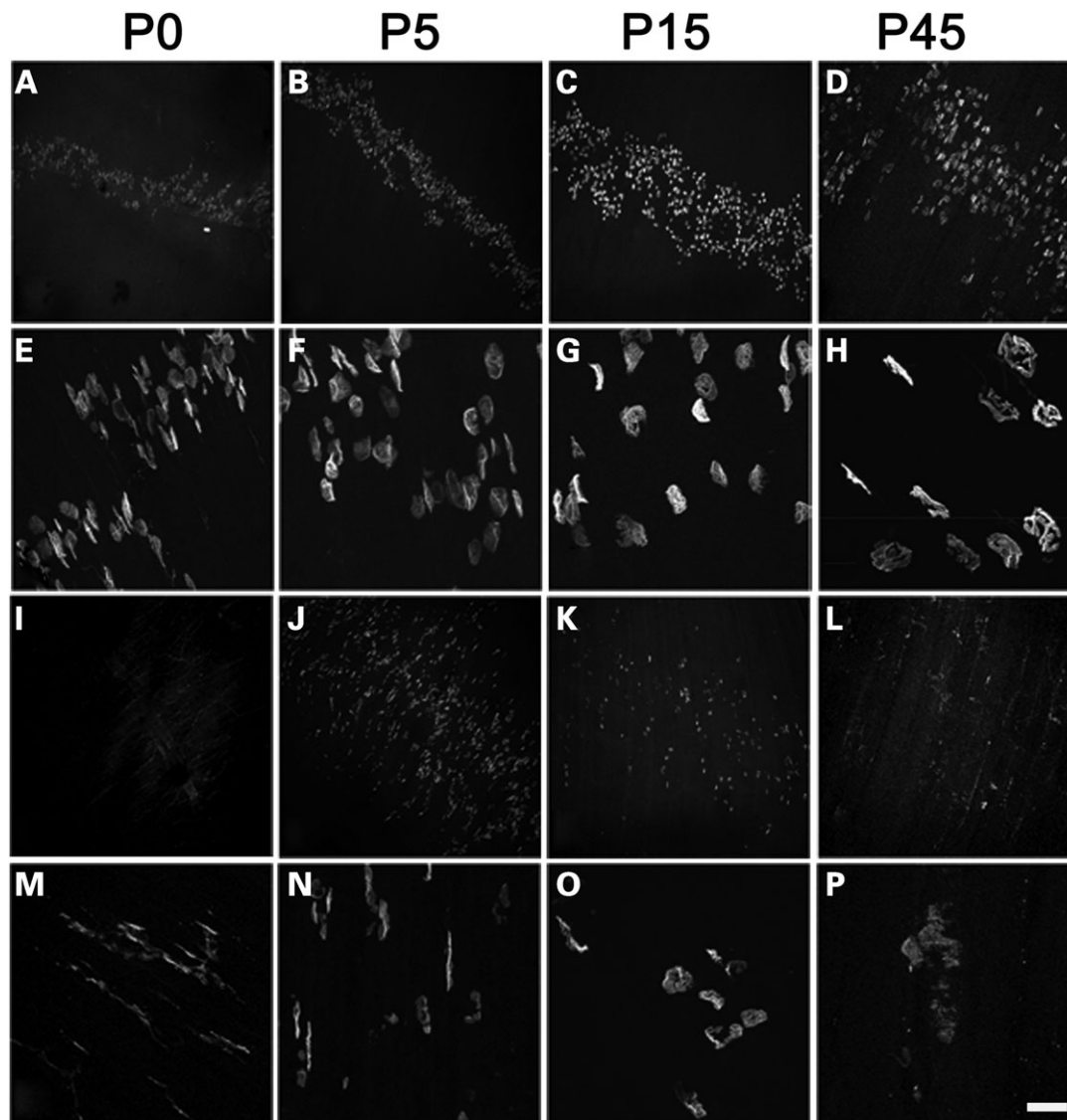
Figure 7. Endplate evolution during post-natal maturation in the diaphragm of WT and *musk*[V789M/−] mice. Endplates from WT (**A–H**) and *musk*[V789M/−] (**I–P**) mouse diaphragms stained with r-bgt at P0 (A, E, I and M), P5 (B, F, J and N), P15 (C, G, K and O) and P45 (D, H, L and P). Scale bar=150 µm (A–D; I–L) and scale bar=20 µm (E–H; M–P). (**Q**) The length (µm) of the longest axis of individual clusters was evaluated in the diaphragm muscle for each genotype at P0. Values are means ± SEM from three mice per genotype (50 AChR clusters per diaphragm). WT mice: 14.93 ± 1.06 µm; musk[V789M/V789M] mice: 14.39 ± 1 µm; *musk*[loxP/−] mice: 15.69 ± 0.13 µm; *musk*[V789M/−] mice: 8.26 ± 1.15 µm (**P ≤ 0.01 versus WT by *t*-test). (**R**) Number of AChR clusters in the diaphragm of WT, *musk*[loxP/−] and *musk*[V789M/−] mice at P15. Data are means ± SEM from three diaphragms per genotype (*P ≤ 0.05 versus WT by *t*-test). (**S**) Representative images obtained from P15 WT and *musk*[V789M/−] mouse diaphragms stained with neurofilament (NF) and AChR, Note that some NMJs appeared to mature normally in *musk*[V789M/−] mice at P15 (upper NMJ), considering the density of AChR-rich regions, the perforation and branching, others displayed progressive loss of AChR-rich domains (lower NMJ), scale bar = 10 µm.

Architectural alteration of nmj in *musk*[V789M/−] mice

In order to analyse the morphological alteration of the NMJs at ultrastructural level in *musk*[V789M/−] mice, we performed electron microscopy analysis on *soleus* muscle of 3-month-old *musk*[V789M/−] and WT mice (Fig. 9). In WT, junctional folds are numerous and well-developed (Fig. 9A). The sarcoplasm containing mitochondria and subsynaptic nuclei but no myofibrils, the so-called sole plate, represents a subsynaptic specialization that may control transcriptional and post-translational regulation at the NMJ. As shown in Figure 9B, post-synaptic membranes in *soleus* muscle of musk[V789M/−] mice presented few junctional folds and the distance between this post-synaptic membrane and the myofibril compartment was reduced. Mitochondria invaded the subsynaptic space and accumulated directly beneath the post-synaptic membrane, whereas subsynaptic nuclei seemed to have disappeared or were disintegrated (Fig. 9B) and in many cases the sole plate was abolished (Fig. 9C). Similar endplate architectural disruption has been observed in several CMSs (16,28).
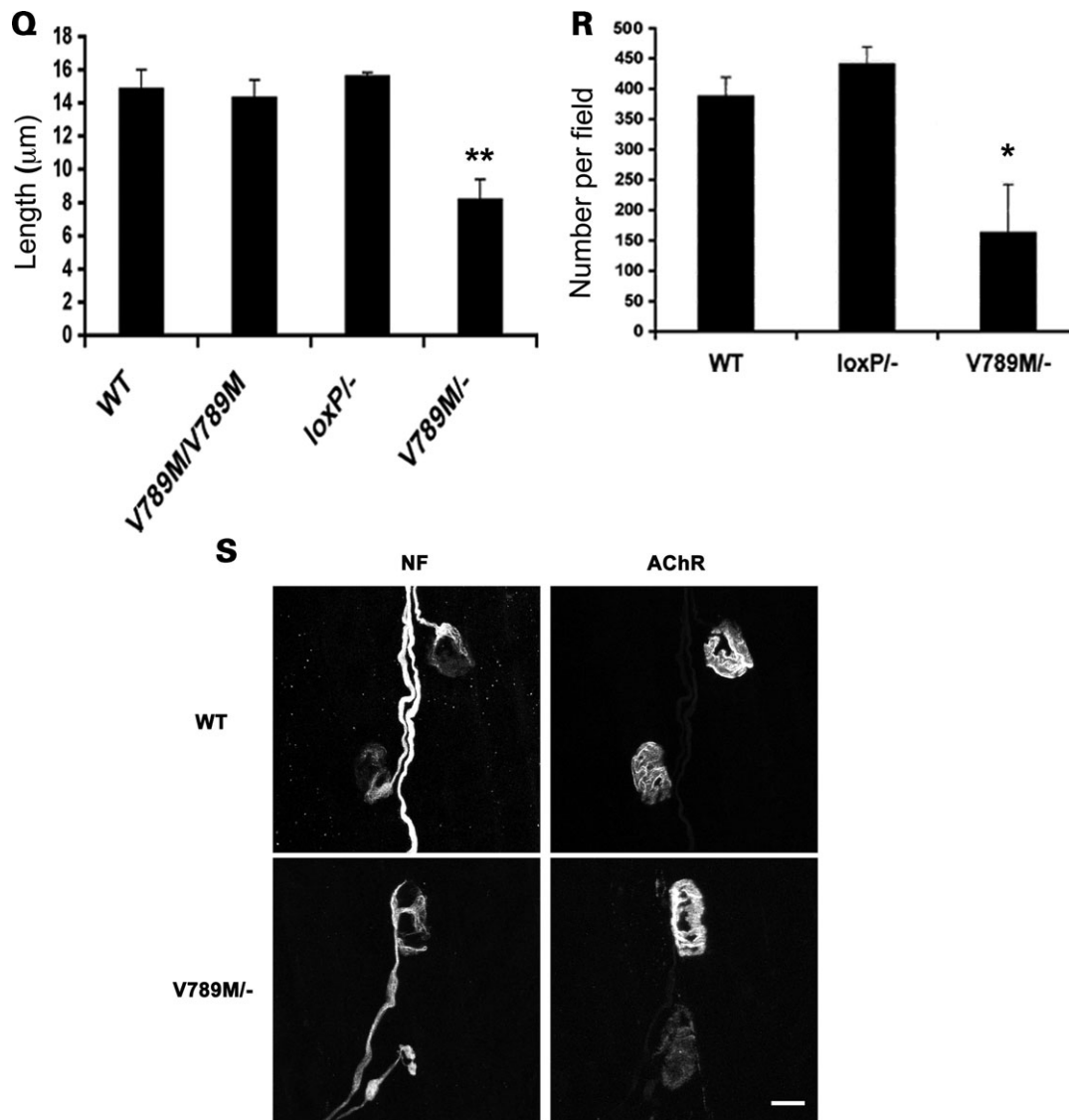
Figure 7. *Continued*

Loss of MuSK expression at NMJS and inactivity-related gene expression in *tibialis anterior* of *musk*[V789M/−] mice

In order to determine whether the expression of MuSK is modified at the post-synaptic sites of *musk*[V789M/−] mice, we performed immunochemistry on TA cryostat sections from P90 WT and *musk*[V789M/−] mice (Fig. 10A–D). As represented in Figure 10C, the level of MuSK at post-synaptic membranes identified by r-bgt (Fig. 10D) was found drastically reduced in *musk*[V789M/−] mice when compared with WT mice (Fig. 10A). In *musk*[V789M/V789M] mice, MuSK was found normally concentrated at the synapses (data not shown).

We performed, then, a quantification of MuSK, AChR ε, α and γ subunit mRNAs by relative real-time RT–PCR on TA muscle extracts. As observed (Fig. 10E), TA from *musk*[V789M/−] mice presented an up-regulation of the expression of MuSK mRNAs compared with WT mice. In contrast to WT, the amount of AChR ε subunit mRNAs was

reduced by half in *musk*[V789M/−] mice (Fig. 10F). In correlation to the up-regulation of MuSK mRNA we found a large increase in AChR α and γ subunit mRNAs was found (Fig. 10G and H, respectively). These results suggested an inactivity- or denervation-related gene expression in TA muscle of *musk*[V789M/−] mice.

DISCUSSION

The *musk*[V789M/−] mouse, a model for MuSK-induced CMS

In the present study, we developed *musk*-knock-in mice carrying the V789M missense mutation that was identified in conjunction with a null mutation in the MUSK human gene in a family with an autosomal recessive CMS (24). We show that, as observed in a MuSK-related patient, the heteroallelic association of the missense mutation located in the kinase domain of
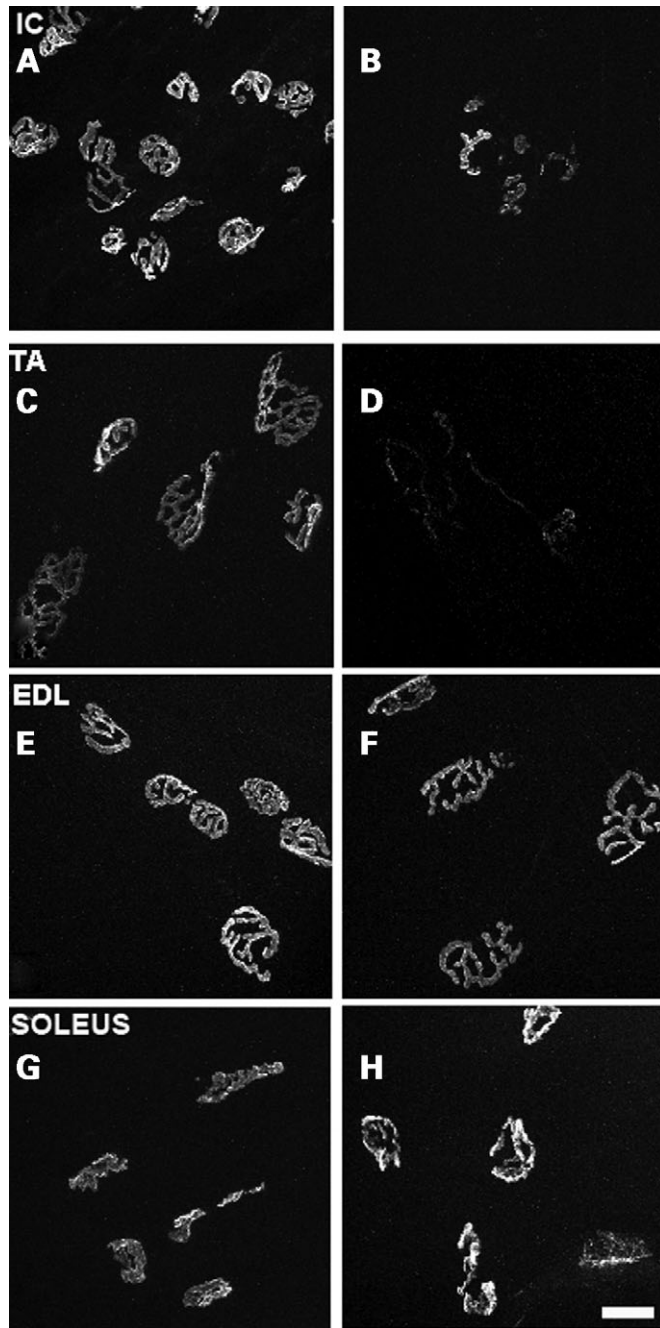
Figure 8. Endplate architecture of the endplates in different muscles of WT and *musk*[V789M/−] mice. Endplates at P45 from WT (**A, C**, **E** and **G**) and *musk*[V789M/−] (**B**, **D**, **F** and **H**) mice of intercostal IC (A and B), *tibialis anterior*, TA (C and D), *extensor digitorum longus*, EDL (E and F) and *soleus* (G and H) muscles stained with r-bgt. Scale bar = 20 μm.

MuSK and an inactivated MuSK allele in *musk*[V789M/−] mice induces a severe fatigable muscle weakness, thus confirming the pathogenicity of the missense mutation in a context of hemizigosity. In adult *musk*[V789M/−] mice, the muscle deficit predominates on axial muscles and leads to a thoracolumbar kyphosis, and the pelvic weakness induces a waddling gait. Such a phenotype can also be observed in other mouse models presenting neuromuscular defects (9,14,29–32).

The V789M mutation by itself at a homozygous state in *musk*[V789M/V789M] mice is not sufficient to induce an abnormal phenotype in locomotion, growth or viability. This is also the case in *musk*^{+/−} or *musk*[loxP/−] mice, where the reduction by half of MuSK failed to lead to any obvious phenotype or abnormalities of the NMJs (3,6,14). These hemizygous mice demonstrate that WT *musk* is not a haploinsufficient gene (33). The presence of the null allele in *musk*[V789M/−] mice, in contrast, discloses the pathogenic character of the V789M missense mutation generating *in fine* a 'MuSK haploinsufficiency'. In these mice, MuSK activity is reduced by both a quantitative defect due to the null allele and a qualitative defect due to the presence of the V789M mutation in the catalytic domain of MuSK. Expression and activity of MuSK at synaptic sites may be further reduced due to the impairment of a positive auto-regulation loop (9,31). As a result of the reduced MuSK activity, normally required to maintain the high AChR density at the NMJ (14), one observes a continuous loss of AChRs and finally a loss of NMJs. Immunohistochemical analysis of MuSK in TA muscle actually shows that MuSK as well as AChR densities are significantly reduced at NMJs of *musk*[V789M/−] mice. In addition, AChR ε subunit transcript levels that are only expressed at subsynaptic nuclei (34) are also significantly reduced. A decrease in ε subunit transcript levels was also observed in the patient carrying the heteroallelic MuSK mutations (24), supporting the view that MuSK activity may be linked to synapse-specific transcription (35). The loss of NMJs on the other hand induces 'denervation-like' changes that cause an increase in α and γ subunit as well as MuSK transcript levels, and similar mRNA increases were again observed in the human patient (24). Additionally, reduction in MuSK activity may also weaken mechanisms involved in the stabilization of NMJs and post-natal maturation such as activation of src family tyrosine kinases (36–41).

Surprisingly, the MuSK-dependent impairment of NMJs develops differently in different muscle. Strongly affected muscle include diaphragm, TA and intercostal muscle, whereas EDL or *soleus* muscles appeared less-sensitive to reduced MuSK activity and deficits may become apparent only at older age. These results suggest that while MuSK activity is necessary in all muscles to maintain NMJ integrity, additional neuronal or muscle-specific modulatory signals are required to control muscle-type-specific properties. The muscle-type-specific effect observed here for MuSK may have also been observed in experimental models of myasthenia gravis (32,42,43). A possible explanation could be that in these muscles, other molecules could reinforce the integrity of the NMJs as observed with β dystroglycan in zebrafish (44). It could also be that the mode of contraction or activity of each muscle influences the maintenance of MuSK at NMJs differently. As a result, endplate AChRs or innervating motoneuron population respond differently to MuSK deficiency (45).

We previously showed *in vitro* (24) that the phosphorylation and AChR aggregating activity of mutated MuSK was reduced in myotubes. Recently, it has been shown that Dok-7 is essential for neuromuscular synaptogenesis through its interaction with MuSK (15). *In vitro* studies indicated that the interaction of Dok-7 and MuSK[V789M] was impaired (15). Even if we could not rule out a defect of interaction with other effectors, the impairment in regulatory interaction between MuSK[V789M]
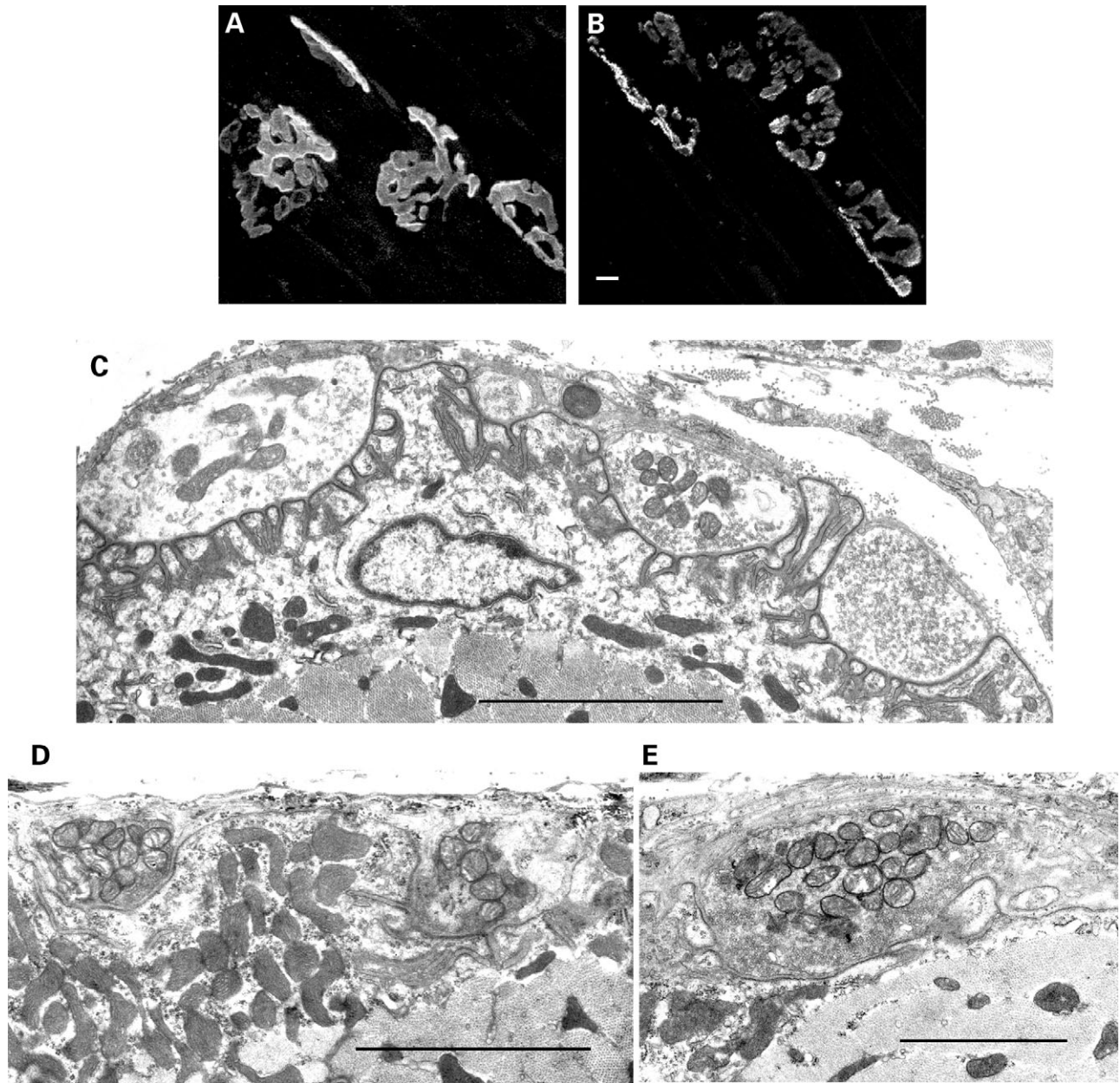
Figure 9. Electron micrographs of NMJs of *soleus* muscle from WT and *musk*[V789M/−] mice. Endplates from WT (**A**) and *musk*[V789M/−] (**B**) mice of *soleus* muscles at P120 stained with r-bgt. Scale bar = 10 μm. (**C**) NMJ at P120 from WT. Scale bar 5 μm. (**D** and **E**) NMJ at P120 of a *musk*[V789M/−] mouse. Scale bars = 2.5 μm.

and Dok-7 could be one possible mechanism leading *in vivo* to the insufficiency in MuSK function in *musk*[V789M/−] mice. As Dok-7 mutations confer a quite particular phenotype in patients (17,18,46,47), it will be interesting to compare our mice with transgenic mice bearing Dok-7 mutations leading to impaired MuSK activity.

Remodelling of the NMJ causes muscle weakness

In diaphragms of adult *musk*[V789M/−] mice, synaptic remodelling is manifested by a severe fragmentation and loss of endplate structure associated with axonal retraction and sprouting.

Such perturbations, indicating 'denervation-like' processes, are likely to induce a profound fatigable muscle weakness as demonstrated by the dramatic waning of muscle tension after tetanic nerve stimulation on isolated hemidiaphragm. Moreover, the diaphragms develop less force and peak twitch and maximum tetanic amplitudes are decreased after direct muscle stimulation and the contraction and half relaxation times of muscle- or nerve-evoked single twitches are prolonged. In this context it is of interest that denervation-induced inactivity of diaphragm has been shown to lead to a decrease in peak twitch and maximum tetanic force as well as prolongation of the time constants of muscle
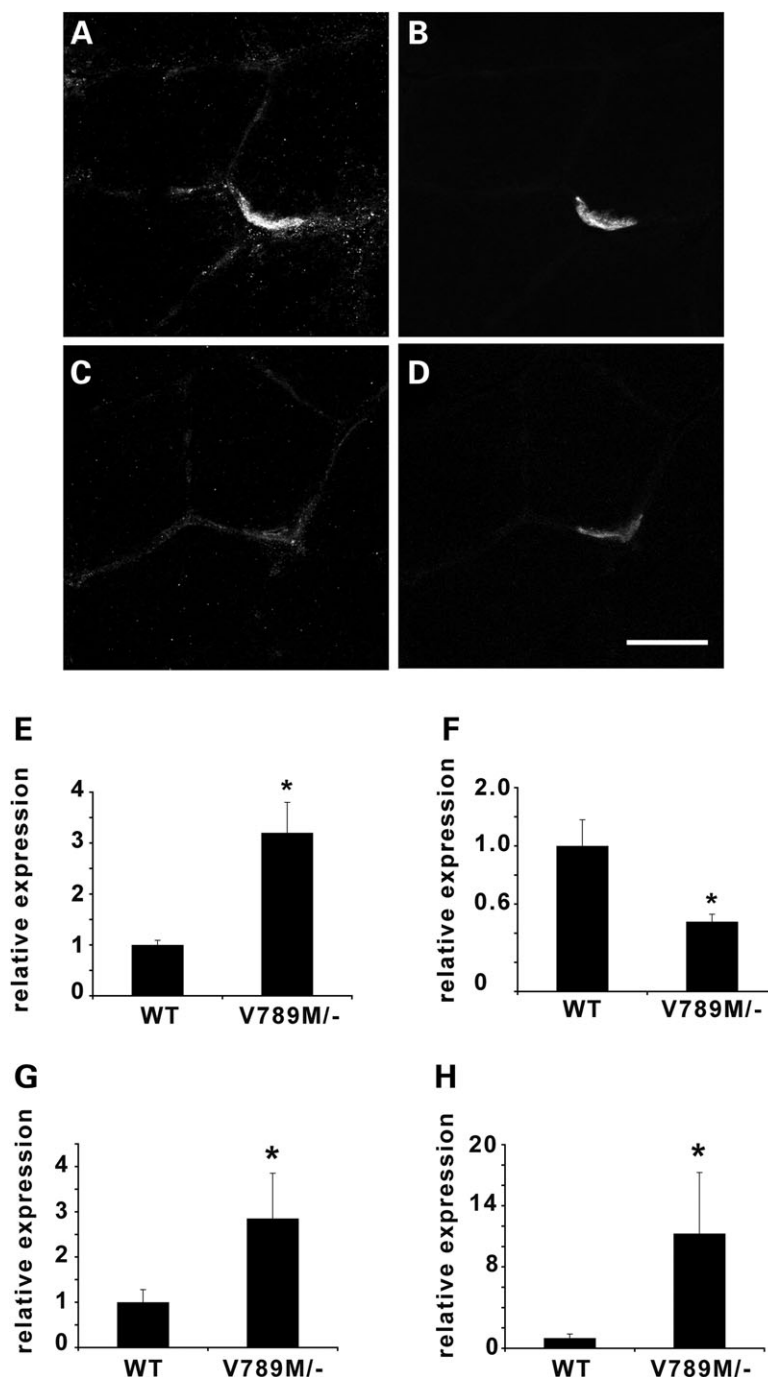
Figure 10. Loss of MuSK at NMJs from *musk*[V789M/−] mouse *tibialis anterior* muscle and inactivity-related gene expression. Immunohistochemistry on tibialis anterior cryostat sections from P90 WT (**A** and **B**) and *musk*[V789M/−] (**C** and **D**) mice for MuSK (A and C) and AChR (B and D). Scale bar = 20 μm. (**E**) MuSK mRNA relative quantification using P90 WT and *musk*[V789M/−] mouse *tibialis anterior*. (**F**) AChR ε subunit mRNA relative quantification for each genotype (**G**) AChR α subunit mRNA relative quantification for each genotype. (**H**) AChR γ subunit mRNA relative quantification for each genotype. Data are means ± SD for five animals per genotype (*$P \leq 0.05$ versus WT by *t*-test).

contraction and relaxation (48,49). As a consequence of a reduction in contraction speed in this muscle, the twitch/tetanus ratio is enhanced (50). The strongly increased fatigability of diaphragm may cause respiratory insufficiency and could be responsible for the premature death of male *musk*[V789M/−] mice between the second and fourth month of life. It should also be noted that respiratory distresses were observed during neonatal period in a patient with MuSK mutations (24).

Impaired neurotransmission

At synaptic contacts of *musk*[V789M/−] hemidiaphragm, the amplitude of MEPPS and their time course is similar to

musk^{V789M/+} hemidiaphragm values suggesting that the local density of adult AChRs is high enough to induce normal spontaneous events. Nonetheless, the amplitude of the EPPS is significantly diminished. Such a reduction in amplitude could result from fewer transmitter quanta being released by a single nerve impulse or from a smaller post-synaptic effect of individual quanta (16). Moreover, it is generally assumed that the quantal content of EPPS is related to the synaptic area (51).

In diaphragm of *musk*^{V789M/−} mice, the mean quantal content is decreased by 40% of the control value in our study. The synaptic contacts as characterized by r-bgt-labelled endplate AChR clusters in close apposition to synaptophysin-stained nerve terminals are clearly reduced in size and the arborized structure of WT endplates is simplified. The reduced pre- and post-synaptic areas could account for reduced MEPPS frequency, lower quantal content and reduced EPP amplitude rather than defects in the process of neuromuscular transmission itself. Pre- and post-synaptic abnormalities have also been discussed as cause of muscle weakness in limb-girdle myasthenic patients (16). It cannot be excluded, however, that there may also be effects on the presynaptic compartment due to impaired retrograde signals induced by MuSK insufficiency.

Developmental changes

In *musk*^{V789M/−} mice, the phenotypic expression of the disease occurs apparently only 3 weeks after birth suggesting that the combination of the V789M mutation with a null allele interferes mainly with the NMJ maturation and maintenance. Embryonic and early post-natal development is obviously not as severely affected as in mice that lack MuSK completely, and that fail to form synapses and therefore die at birth (3–6). Nevertheless, it is anticipated that MuSK insufficiency modulates early steps in synapse formation and development. At this stage, our results show that at birth endplates are not concentrated within a narrow band but are spread out over a wide region and the size of the clusters is significantly reduced. These conspicuous differences to WT diaphragms indicate that the initiation and/or the differentiation programmes of the NMJs during development in *musk*^{V789M/−} mouse diaphragm are modified. However, the residual activity conferred by MuSK^{V789M} is sufficient to circumvent the death of these animals at birth. All together, our results indicate that the 'MuSK haploinsufficiency' in *musk*^{V789M/−} mice during development may well be a limiting factor in agrin/MuSK/rapsyn signalling pathways that regulate AChR prepatterning as well as synapse formation and stabilization.

In summary, the hemizygous *musk*^{V789M/−} mice that we generated develop muscle weakness similar to patients suffering from CMS. This heteroallelic combination of both mutations create a MuSK haploinsufficiency and leads to a defect in the patterning and the aggregation of AChRs at NMJ as well as the maintenance of these NMJs at adulthood. The *musk*^{V789M/−} mice represent a valuable tool to dissect the MuSK signalling pathway and possibly to develop new pharmacological and genetic treatment strategies for a CMS due to MuSK mutations. With regard to the apparent normal phenotype of *musk*^{V789M/V789M} mice, a possible strategy in

musk^{V789M/−} mice should be to compensate the insufficiency of MuSK function by stimulating the synapse-specific transcription and production of MuSK^{V789M} at the synapses.

MATERIALS AND METHODS

All experiments on mice were performed in accordance with European Community guidelines for laboratory animal handling.

Generation of musk^{V789M/V789M} and musk^{V789M/−} mice

The construction of the gene-targeting vector used for homologous recombination was described in Hesser *et al.* (14), and contained a neomycin-resistant cassette (*neo*) and *loxP* sites flanking the exon encoding the sequence of the MuSK kinase domain. This targeting vector was digested by *Bam*HI creating a 3.2 kb fragment bearing the sequence of the catalytic kinase domain. This fragment was subcloned using Topo^R cloning vector (Invitrogen, Karlsruhe, Germany) and the G to A transition at nucleotide 2365 of the coding sequence in the exon encoding the catalytic domain of MuSK (c.2365G→A; NCBI accession number: NM_010944) was introduced using the site-directed mutagenesis kit (Stratagene, La Jolla, CA, USA) with the following primers: forward 5′-GTATGGGC CTATGGTATGGTCCTCTGGGAGA-3′ and reverse 5′-TCT CCCAGAGGACCATACCATAGGCCCATAC-3′.

The correct mutated fragment was then re-introduced in the gene-targeting vector. The *Xho*I site created at the 3′ end of the targeting vector was used for linearization. ES cells were used for gene targeting and transfected with 25 μg of the *Xho*I-linearized targeting construct by electroporation (300 V, 1200 μF). Cells were subjected to selection with G 418^R (335–350 μg/ml) and clones were picked after 14 days of selection. PCR, Southern blot and sequencing of *Hin*dIII-digested fragment genomic DNA identified targeted clones correctly. ES cells of two clones were injected into blastocysts derived from C57Bl/6J mice. Germline transmission was achieved and breeding of heterozygous mice resulted in homozygous *musk*^{V789M/V789M} mice. The breeding of these homozygous mice with musk[±] mice (14) was used to generate 'hemizygous' *musk*^{V789M/−} mice.

Primers for identifying the *musk*^{V789M} and WT alleles were: 662 (forward) 5′-CTGGTCCTCCACCCCTGTC-3′ and 852 (reverse) 5′-TGTAGGAACGTAACCGGGATG-3′. Primers for detecting *musk*[−] allele were: 848 (forward) 5′-CTCTT GCAAGAAATATGTTGTCTCAGGC-3′ and 852 (reverse) 5′-TGTAGGAACGTAACCGGGATG-3′.

PCR conditions were: 1 cycle 95°C for 2 min; 30 cycles of 95°C for 30 s, 60°C for 30 s, 72°C for 90 s; followed by one cycle of 72°C for 10 min. The PCR products were separated on agarose gels, visualized with ethidium bromide.

Computed Tomography scan analysis

A prototype computed tomography scanner was used for gating experiments. It consisted of a flat-panel detector and a modified x-ray tube both mounted on a multi-slice computed tomography gantry. The flat-panel detector (PaxScan

4030CB, Varian Medical Systems), consists of 2048×1536 detector pixels on an active area of 40×30 cm^2 resulting in a pixel size of 194^2 μm^2. X-ray photons are converted to light photons in a scintillation layer of caesium-iodine crystals which are subsequently detected by the photodiodes of the amorphous silicon waver. Taking the geometry of the scanner setup into consideration the scanner's total scan field-of-view is $25 \times 25 \times 18$ cm^3. The resolution of the scanner is 24 line pairs/cm at 10% modulation transfer function (measured by scanning a 100 μm tungsten wire phantom) for every spatial direction, which can be translated in a minimal detectable feature size of 200 μm. Scanner rotation times can be varied from 2 to 20 s in steps of 1 s, the maximum total scan time being 80 s. The x-ray tube has been modified to extend the anode angle in order to suite the requirements of cone-beam computed tomography. Furthermore, the focal spot size was reduced to 0.5 mm to reduce the effect of penumbral blurring. An even smaller focal spot would result in a reduced photon flux and would therefore require longer exposure times. Total scan time was 80 s with a rotation time of 5 s resulting in 16 full rotations per scan. A tube voltage of 80 kV and a tube current of 50 mA with continuous radiation were selected. Motion-gated as well as ungated reconstructions were performed. The reconstruction field-of-view was 4.5 cm transaxially with a reconstruction matrix of 512×512 pixels and an axial slice spacing 0.2 mm resulting in a voxel size of $0.08 \times 0.08 \times 0.2$ mm^3. A sharp reconstruction kernel (H80s) was used for image reconstruction. Reconstructed volume datasets have been fitted with a DICOM 3 header and have been imported into a standard medial images post-processing workstation (Leonardo, Siemens, Medical Solutions, Forchheim, Germany). The DICOM image data was then post-processed using volume rendering with a musculoskeletal bone transfer function to assess the structure of the back bone.

Grip strength measurement

A computerized electronic pull-strain gauge (Columbus Instruments, Columbus, OH, USA) was used to determine the forelimb grip strength. Animals were allowed to grasp the triangular ring and were pulled horizontally until the grip was released. Three measurements were performed per animal and the average of these three measurements was used for statistical evaluation of mean and SD. No significant differences in this test were detected between male and female.

Rotarod test

Motor coordination and balance were measured by performance on the rotarod. The rotarod test was performed using an accelerating rotarod and consisted of placing a mouse on a rotating drum (3 cm in diameter) and measuring the time for which each animal was able to maintain its balance on the rod. The speed of the rotarod accelerated from 4 to 40 rpm over a 5-min period. The mice were trained on five consecutive days, and the latency to falls was estimated as index of performance.

Ex vivo isometric tension analyses

3 month-old mice ($musk^{V789M/+}$ and $musk^{V789M/-}$) were anesthetized with Isoflurane (AErrane®, Baxter S.A., Lessines, Belgium) inhalation, and euthanized by dislocation of the cervical vertebrae followed by immediate exsanguination.

Mouse hemidiaphragm muscles were mounted in a silicone-lined bath filled with Krebs–Ringer solution of the following composition: 154 mM NaCl, 5 mM KCl, 2 mM CaCl$_2$, 1 mM MgCl$_2$, 11 mM glucose and 5 mM HEPES (buffered at pH 7.4 with NaOH), continuously perfused with O$_2$ at $22 \pm 0.5°$C. One of the hemidiaphragm tendons was securely anchored onto the silicone-coated bath via stainless steel pins, while the other tendon was tied with silk thread, via an adjustable stainless steel hook, to an FT03 isometric force transducer (Grass Instruments, West Warwick, RI, USA). Muscle twitches and tetanic contractions were evoked either by stimulating the motor nerve via a suction microelectrode adapted to the diameter of the nerve, with supramaximal current pulses of 0.15 ms duration, at frequencies indicated in the text, or by direct electrical stimulation with an electrode assembly placed along the length of the fibres. The resting tension was adjusted for each preparation, investigated with a mobile micrometer stage (to allow incremental adjustments of muscle length) in order to obtain maximal contractile responses upon indirect and direct muscle stimulation. The resting tension was monitored during the whole duration of experiments. Signals from the isometric transducer were amplified, collected and digitized with the aid of a computer equipped with an analogue to digital interface board (Digidata 1200, Axon Instruments, Union City, CA, USA) using a software kindly provided by Dr John Dempster (Department of Physiology and Pharmacology, University of Strathclyde, Scotland).

Ex vivo electrophysiological studies

Electrophysiological recordings were carried out using conventional techniques (52). Membrane and synaptic potentials were recorded from endplate regions at $22 \pm 0.5°$C with intracellular microelectrodes (filled with 3 M KCl solution, $8-12$ MΩ resistance) and an Axoclamp-2A system (Axon Instruments). The phrenic nerve was stimulated by a suction electrode with current pulses of 0.15 ms duration and supramaximal voltage (typically $3-8$ V) at 0.1 Hz unless otherwise specified. Electrical signals were collected after amplification and digitized at a sampling rate of 25 kHz with a computer equipped with an analogue to digital interface board (see earlier). Studies on nerve-evoked EPPs were performed in standard physiological solution containing 1.6 μM μ-conotoxin-GIIIB (Alomone Labs, Jerusalem, Israel), a selective muscle Na$^+$ channel blocker, to inhibit the generation of muscle action potentials (53). The amplitudes of full-sized EPPs and MEPPs recorded on NMJs were normalized to a membrane potential of -75 mV. EPP amplitudes were corrected for non-linear summation (54). The quantal content of full-sized EPPs was calculated at each NMJ by the direct method, which consists in dividing the mean normalized and corrected EPP amplitude by the mean normalized MEPP amplitude. Giant MEPPs were excluded from the amplitude

analysis since they did not enter in the composition of evoked EPPs. Usually, 20 consecutive EPPs and 50–80 MEPPs were used in the calculations.

Statistic analyses

Data expressed as the mean $\pm$ SEM. Student's *t*-test (two-tailed) was used to determine the statistical significance of the difference between *musk*^V789M/+ and *musk*^V789M/− parameters values studied. Differences were considered as significant when $P < 0.05$.

Whole-mount staining of diaphragms

Muscles were dissected and fixed for 1 h with 1% formaldehyde in phosphate-buffered saline (PBS). They were incubated in 0.1 M glycine/PBS, washed in PBS and then incubated in 2% bovine serum albumin (BSA) in PBS. Synaptophysin (1/50, Zymed Laboratories, Inc.) or NF 150 (1/500, Chemicon) polyclonal antibodies were incubated overnight in 2% BSA/PBS. Excess of antibodies were removed washing the tissue three times in PBS. Secondary FITC-coupled anti-rabbit goat antibodies (1/100, Mobitech) were incubated overnight with tetramethylrhodamine-conjugated a-bungarotoxin (r-bgt, 2 μg/ml; Molecular Probes, Leiden, The Netherlands) in 2% BSA in PBS. After washing in 2% BSA/PBS, muscles were mounted in CITIFLUOR for microscopic analysis. Confocal image series were recorded on a Leica confocal laser scanning unit, TCS NT, which was coupled to a Leica DM IRB microscope. The image series and quantification were processed using TCS NT software (Leica, Bensheim, Germany). Number of AChR clusters was determined from images taken with a ×10 objective; AChR cluster size was measured from images taken with a ×63 objective.

Immunohistochemistry

For immunohistochemistry, *tibialis anterior* muscles of adult mice were collected and immediately frozen in liquid nitrogen-cooled isopentane. Eight-micrometre thick cryostat sections were collected on microscope slides, dried for 30 min and rehydrated in PBS for 5 min. Non-specific binding was blocked with 2% BSA in PBS for 1 h at room temperature. Then, sections were incubated overnight at 4°C with MuSK rabbit polyclonal antibodies (194T, a gift from Dr Markus Rüegg) diluted in PBS with 2% BSA. After washing, sections were incubated with FITC-coupled anti-rabbit goat antibodies (1/100, Mobitech) and r-bgt (1/500). The slides were washed with PBS and mounted in CITI-FLUOR for microscopic analysis.

Electron microscopy

For ultrastructural analysis, *soleus* muscles were dissected and immediately fixed for 1 h in 4% paraformaldehyde. After a short wash with PBS, the muscles were incubated in PBS containing r-bgt (dilution 1/500) for 1 h, washed and then the endplate-containing tissue blocks were cut under the fluorescence microscope. Tissue blocks were post-fixed overnight at 4°C in a calcium-free buffer (100 mM cacodylate, pH 7.4) using 2.5% glutaraldehyde and 2% paraformaldehyde. After washing with PBS, the samples were incubated for 2 h at room temperature in 2% osmium tetroxide and 1.5% potassium-hexacyanoferrate in water. Specimens were washed and incubated overnight at 4°C in 4% uranylacetate in 25% methanol and water. Following standard procedures for dehydration, the tissues were embedded in SPURR medium. Ultrasections were contrasted in uranylacetate for at least 20 min and in lead citrate for 5 min. Sections were viewed in a Philips EM 400T and images were documented on Kodak S0-163.

Relative quantitative real-time PCR

RNA was isolated from P90 normal and mutant hindlimb muscles using Trizol reagent (Invitrogen). First-strand cDNA was synthesized from 5 μg of total RNA using reverse transcriptase and 1 μl of pol(N)$_6$ random hexamer (Amersham Pharmacia, Freiburg, Germany). Relative quantification of PCR product synthesis was performed using Applied Biosystems 7500 Real-Time PCR system and assay-on-demands according to the recommendations of the manufacturer (Applied Biosystems). The expression levels obtained were normalized to the transcription level of the housekeeping enzyme glyceraldehyde-3-phosphate dehydrogenase (GAPDH). Assay-on-demand references were for MuSK: Mm00448006_m1; AChR γ subunit: Mm00437417_m1; AChR ε subunit: Mm00437411_m1; AChR α subunit: Mm00431627_m1; GAPDH: Mm99999915_g1;

REFERENCES

1. Sanes, J.R. and Lichtman, J.W. (2001) Induction, assembly, maturation and maintenance of a postsynaptic apparatus. *Nat. Rev. Neurosci.*, **2**, 791–805.
2. Witzemann, V. (2006) Development of the neuromuscular junction. *Cell Tissue Res.*, **326**, 263–271.
3. DeChiara, T.M., Bowen, D.C., Valenzuela, D.M., Simmons, M.V., Poueymirou, W.T., Thomas, S., Kinetz, E., Compton, D.L., Rojas, E., Park, J.S. *et al.* (1996) The receptor tyrosine kinase MuSK is required for neuromuscular junction formation *in vivo*. *Cell*, **85**, 501–512.

4. Gautam, M., Noakes, P.G., Moscoso, L., Rupp, F., Scheller, R.H., Merlie, J.P. and Sanes, J.R. (1996) Defective neuromuscular synaptogenesis in agrin-deficient mutant mice. *Cell*, **85**, 525–535.

5. Gautam, M., DeChiara, T.M., Glass, D.J., Yancopoulos, G.D. and Sanes, J.R. (1999) Distinct phenotypes of mutant mice lacking agrin, MuSK, or rapsyn. *Brain Res. Dev. Brain Res.*, **114**, 171–178.

6. Lin, W., Burgess, R.W., Dominguez, B., Pfaff, S.L., Sanes, J.R. and Lee, K.F. (2001) Distinct roles of nerve and muscle in postsynaptic differentiation of the neuromuscular synapse. *Nature*, **410**, 1057–1064.

7. Yang, X., Arber, S., William, C., Li, L., Tanabe, Y., Jessell, T.M., Birchmeier, C. and Burden, S.J. (2001) Patterning of muscle acetylcholine receptor gene expression in the absence of motor innervation. *Neuron*, **30**, 399–410.

8. Sander, A., Hesser, B.A. and Witzemann, V. (2001) MuSK induces *in vivo* acetylcholine receptor clusters in a ligand-independent manner. *J. Cell. Biol.*, **155**, 1287–1296.

9. Kim, N. and Burden, S.J. (2008) MuSK controls where motor axons grow and form synapses. *Nat. Neurosci.*, **11**, 19–27.

10. Lin, S., Landmann, L., Ruegg, M.A. and Brenner, H.R. (2008) The role of nerve- versus muscle-derived factors in mammalian neuromuscular junction formation. *J. Neurosci.*, **28**, 3333–3340.

11. Koenen, M., Peter, C., Villarroel, A., Witzemann, V. and Sakmann, B. (2005) Acetylcholine receptor channel subtype directs the innervation pattern of skeletal muscle. *EMBO Rep.*, **6**, 570–576.

12. Misgeld, T., Kummer, T.T., Lichtman, J.W. and Sanes, J.R. (2005) Agrin promotes synaptic differentiation by counteracting an inhibitory effect of neurotransmitter. *Proc. Natl. Acad. Sci. USA*, **102**, 11088–11093.

13. Lin, W., Dominguez, B., Yang, J., Aryal, P., Brandon, E.P., Gage, F.H. and Lee, K.F. (2005) Neurotransmitter acetylcholine negatively regulates neuromuscular synapse formation by a Cdk5-dependent mechanism. *Neuron*, **46**, 569–579.

14. Hesser, B.A., Henschel, O. and Witzemann, V. (2006) Synapse disassembly and formation of new synapses in postnatal muscle upon conditional inactivation of MuSK. *Mol. Cell. Neurosci.*, **31**, 470–480.

15. Okada, K., Inoue, A., Okada, M., Murata, Y., Kakuta, S., Jigami, T., Kubo, S., Shiraishi, H., Eguchi, K., Motomura, M. *et al.* (2006) The muscle protein Dok-7 is essential for neuromuscular synaptogenesis. *Science*, **312**, 1802–1805.

16. Slater, C.R., Fawcett, P.R., Walls, T.J., Lyons, P.R., Bailey, S.J., Beeson, D., Young, C. and Gardner-Medwin, D. (2006) Pre- and post-synaptic abnormalities associated with impaired neuromuscular transmission in a group of patients with 'limb-girdle myasthenia'. *Brain*, **129**, 2061–2076.

17. Beeson, D., Higuchi, O., Palace, J., Cossins, J., Spearman, H., Maxwell, S., Newsom-Davis, J., Burke, G., Fawcett, P., Motomura, M. *et al.* (2006) Dok-7 mutations underlie a neuromuscular junction synaptopathy. *Science*, **313**, 1975–1978.

18. Palace, J., Lashley, D., Newsom-Davis, J., Cossins, J., Maxwell, S., Kennett, R., Jayawant, S., Yamanashi, Y. and Beeson, D. (2007) Clinical features of the DOK7 neuromuscular junction synaptopathy. *Brain*, **130**, 1507–1515.

19. Hamuro, J., Higuchi, O., Okada, K., Ueno, M., Iemura, S., Natsume, T., Spearman, H., Beeson, D. and Yamanashi, Y. (2008) Mutations causing DOK7 congenital myasthenia ablate functionals motifs in Dok-7. (2008). *J. Biol. Chem.*, **283**, 5518–5524.

20. Slater, C.R. (2003) Structural determinants of the reliability of synaptic transmission at the vertebrate neuromuscular junction. *J. Neurocytol.*, **32**, 505–522.

21. Engel, A.G. and Sine, S.M. (2005) Current understanding of congenital myasthenic syndromes. *Curr. Opin. Pharmacol.*, **5**, 308–321.

22. Müller, J.S., Mihaylova, V., Abicht, A. and Lochmüller, H. (2007) Congenital myasthenic syndromes: spotlight on genetic defects of neuromuscular transmission. *Expert Rev. Mol. Med.*, **9**, 1–20.

23. Beeson, D., Webster, R., Cossins, J., Lashley, D., Spearman, H., Maxwell, S., Slate, C.R., Newsom-Davis, J., Palace, J. and Vincent, A. (2008) Congenital myasthenic syndromes and the formation of the neuromuscular junction. *Ann. N. Y. Acad. Sci.*, **1132**, 99–103.

24. Chevessier, F., Faraut, B., Ravel-Chapuis, A., Richard, P., Gaudon, K., Bauché, S., Prioleau, C., Herbst, R., Goillot, E., Ioos, C. *et al.* (2004) MUSK, a new target for mutations causing congenital myasthenic syndrome. *Hum. Mol. Genet.*, **13**, 3229–3240.

25. Slater, C.R. (1982) Postnatal maturation of nerve-muscle junctions in hindlimb muscles of the mouse. *Dev. Biol.*, **94**, 11–22.

26. Marques, M.J., Conchello, J.A. and Lichtman, J.W. (2000) From plaque to pretzel: fold formation and acetylcholine receptor loss at the developing neuromuscular junction. *J. Neurosci.*, **20**, 3663–3675.

27. Kummer, T.T., Misgeld, T., Lichtmann, J.W. and Sanes, J.R. (2004) Nerve-independent formation of a topologically complex postsynaptic apparatus. *J. Cell. Biol.*, **164**, 1077–1087.

28. Engel, A.G., Ohno, K. and Sine, S. (2003) Congenital myasthenic syndromes: progress over the past decade. *Muscle Nerve*, **27**, 4–25.

29. Rafael, J.A., Tinsley, J.M., Potter, A.C., Deconinck, A.E. and Davies, K.E. (1998) Skeletal muscle-specific expression of a utrophin transgene rescues utrophin-dystrophyn deficient mice. *Nat. Genet*, **19**, 79–82.

30. Laws, N. and Hoey, A. (2004) Progression of kyphosis in mdx mice. *J. Appl. Physiol.*, **97**, 1970–1977.

31. Hippenmeyer, S., Huber, R.M., Ladle, D.R., Murphy, K. and Arber, S. (2007) ETS transcription factor Erm controls subsynaptic gene expression in skeletal muscles. *Neuron*, **55**, 726–740.

32. Cole, R.N., Reddel, S.W., Gervásio, O.L. and Phillips, W.D. (2008) Anti-MuSK patient antibodies disrupt the mouse neuromuscular junction. *Ann. Neurol.*, **63**, 782–789.

33. Deutschbauer, A.M., Jaramillo, D.F., Proctor, M., Kumm, J., Hillenmeyer, M.E., Davis, R.W., Nislow, C. and Giaever, G. (2005) Mechanisms of haploinsufficiency revealed by genome-wide profiling in yeast. *Genetics*, **169**, 1915–1925.

34. Brenner, H.R., Witzemann, V. and Sakmann, B. (1990) Imprinting of acetylcholine receptor messenger RNA accumulation in mammalian neuromuscular synapses. *Nature*, **344**, 544–547.

35. Jaworski, A. and Burden, S.J. (2006) Neuromuscular synapse formation in mice lacking motor neuron- and skeletal muscle-derived Neuregulin-1. *J. Neurosci.*, **26**, 655–661.

36. Smith, C.L., Mittaud, P., Prescott, E.D., Fuhrer, C. and Burden, S.J. (2001) Src, Fyn and Yes are not required for neuromuscular synapse formation but are necessary for stabilization of agrin-induced acetylcholine receptors. *J. Neurosci.*, **21**, 3151–3160.

37. Mohamed, A.S., Rivas-Plata, K.A., Kraas, J.R., Saleh, S.H. and Swope, S.L. Src-class kinases act within the agrin/MuSK pathway to regulate acetylcholine receptor phosphorylation, cytoskeletal anchoring, and clustering. *J. Neurosci.*, **21**, 3806–3818.

38. Mittaud, P., Camilleri, A.A., Willmann, R., Erb-Vögtli, S., Burden, S.J. and Fuhrer, C. (2004) A single pulse of agrin triggers a pathway that acts to cluster acetylcholine receptors. *Mol. Cell. Biol.*, **24**, 7841–7854.

39. Sadasivam, S., Willmann, R., Lin, S., Erb-Vögtli, S., Kong, X.C., Rüegg, M.A. and Fuhrer, C. (2005) Src-family kinases stabilize the neuromuscular synapse *in vivo* via protein interactions, phosphorylation, and cytoskeletal linkage of acetylcholine receptors. *J. Neurosci.*, **25**, 10479–10493.

40. Gervásio, O.L., Armson, P.F. and Phillips, W.D. (2007) Developmental increase in the amount of rapsyn per acetylcholine receptor promotes possynaptic receptor packing and stability. *Dev. Biol.*, **305**, 262–275.

41. Brockenhausen, J., Cole, R.N., Gervásio, O.L., Ngo, S.T., Noakes, P.G. and Phillips, W.D. (2008) Neural agrin increases postsynaptic ACh receptor packing by elevating rapsyn protein at the mouse neuromuscular synapse. *Dev. Neurobiol.*, **68**, 1153–1169.

42. Jha, S., Xu, K., Maruta, T., Oshima, M., Mosier, D.R., Atassi, M.Z. and Hoch, W. (2006) Myasthenia gravis induced in mice by immunization with the recombinant extracellular domain of rat muscle-specific kinase (MuSK). *J. Neuroimmunol.*, **175**, 107–117.

43. Xu, K., Jha, S., Hoch, W. and Dryer, S.E. (2006) Delayed synapsing muscles are more severely affected in an experimental model of MuSK-induced myasthenia gravis. *Neuroscience*, **143**, 655–659.

44. Lefebvre, J.L., Jing, L., Becafico, S., Franzini-Armstrong, C. and Granato, M. (2007) Differential requirement for MuSK and dystroglycan in generating patterns of neuromuscular innervation. *Proc. Natl. Acad. Sci. USA*, **104**, 2483–2488.

45. Pun, S., Santos, A.F., Saxena, S., Xu, L. and Caroni, P. (2006) Selective vulnerability and pruning of phasic motoneuron axons in motoneuron disease alleviated by CNTF. *Nat. Neurosci.*, **9**, 408–419.

46. Müller, J.S., Herczegfalvi, A., Vilchez, J.J., Colomer, J., Bachinski, L.L., Mihaylova, V., Santos, M., Schara, U., Deschauer, M., Shevell, M. *et al.* (2007) Phenotypical spectrum of DOK7 mutations in congenital myasthenic syndromes. *Brain*, **130**, 1497–1506.

47. Anderson, J.A., Ng, J.J., Bowe, C., McDonald, C., Richman, D.P., Wollmann, R.L. and Maselli, R.A. (2008) Variable phenotypes associated with mutations in Dok-7. *Muscle Nerve*, **37**, 448–456.

48. Zhan, W.Z., Miyata, H., Prakash, Y.S. and Sieck, G.C. (1997) Metabolic and phenotypic adaptations of diaphragm muscle fibers with inactivation. *J. Appl. Physiol.*, **82**, 1145–1153.

49. Rowley, K.L., Mantilla, C.B. and Sieck, G.C. (2005) Respiratory muscle plasticity. *Respir. Physiol. Neurobiol.*, **147**, 235–251.

50. Seki, K., Taniguchi, Y. and Narusawa, M. (2001) Alteration in contractile properties of human skeletal muscle induced by joint immobilization. *J. Physiol.*, **530**, 521–532.

51. Wood, S.J. and Slater, C.R. (2001) Safety factor at the neuromuscular junction. *Prog. Neurobiol*, **64**, 393–429.

52. Minic, J., Chatonnet, A., Krejci, E. and Molgó, J. (2003) Butyrylcholinesterase and acetylcholinesterase activity and quantal transmitter release at normal and acetylcholinesterase knockout mouse neuromsucular junctions. *Br. J. Pharmacol.*, **138**, 177–187.

53. Cruz, L., Gray, W., Olivera, B., Zeikus, R., Kerr, L., Yoshikami, D. and Moczydlowski, E. (1985) Conus geographus toxins that discriminate between neuronal and muscle sodium channels. *J. Biol. Chem.*, **260**, 9280–9288.

54. McLachlan, E.M. and Martin, A.R. (1981) Non Linear summation of end-plate potentials in the frog and mouse. *J. Physiol.*, **311**, 307–324.